

PHILOSOPHICAL TRANSACTIONS OF THE ROYAL SOCIETY A

MATHEMATICAL, PHYSICAL AND ENGINEERING SCIENCES

Stochastic subspace identification of modal parameters during ice-structure interaction

Journal:	<i>Philosophical Transactions A</i>
Manuscript ID	RSTA-2019-0030.R1
Article Type:	Research
Date Submitted by the Author:	n/a
Complete List of Authors:	Nord, Torodd Skjerve; Norges teknisk-naturvitenskapelige universitet, Sustainable Arctic Marine and Coastal Technology (SAMCoT), Centre for Research-based Innovation (CRI) Wiig Petersen, Øyvind ; Norges teknisk-naturvitenskapelige universitet, Department of Structural Engineering Hendrikse, Hayo; Technische Universiteit Delft
Issue Code (this should have already been entered but please contact the Editorial Office if it is not present):	HERITAGE
Subject:	Structural engineering < ENGINEERING AND TECHNOLOGY, Civil engineering < ENGINEERING AND TECHNOLOGY, Mechanical engineering < ENGINEERING AND TECHNOLOGY, Ocean engineering < ENGINEERING AND TECHNOLOGY
Keywords:	Ice-structure interaction, system identification, subspace methods, uncertainty quantification

SCHOLARONE™
Manuscripts

Author-supplied statements

Relevant information will appear here if provided.

Ethics

Does your article include research that required ethical approval or permits?:

This article does not present research with ethical considerations

Statement (if applicable):

CUST_IF_YES_ETHICS :No data available.

Data

It is a condition of publication that data, code and materials supporting your paper are made publicly available. Does your paper present new data?:

Yes

Statement (if applicable):

The data accessibility is handled by the Hamburg ship model basin (HSVA).
www.hsva.de

Conflict of interest

I/We declare we have no competing interests

Statement (if applicable):

CUST_STATE_CONFLICT :No data available.

Authors' contributions

This paper has multiple authors and our individual contributions were as below

Statement (if applicable):

T.S.N. performed the simulations, identifications, and data analysis and drafted the manuscript.

H.H. conducted the simulations with the ice model.

Ã~.W.P. performed the data analysis.

Stochastic subspace identification of modal parameters during ice-structure interaction

Torodd S. Nord^{1,*}, Øyvind W. Petersen² and Hayo Hendrikse³

¹*Sustainable Arctic Marine and Coastal Technology (SAMCoT), Centre for Research-based Innovation (CRI), Norwegian University of Science and Technology, Trondheim, Norway*

²*Department of Structural Engineering, Norwegian University of Science and Technology, Trondheim, Norway*

³*Delft University of Technology, the Netherlands*

Keywords: Ice-structure interaction, system identification, subspace methods, uncertainty quantification

Summary

1 Identifying the modal parameters of structures located in ice-infested waters may be challenging due to the
2 interaction between the ice and structure. In this study, both simulated data from a state-of-the-art ice-
3 structure interaction model and measured data of ice-structure interaction were both used in conjunction with
4 a covariance-driven stochastic subspace identification method to identify the modal parameters and their
5 corresponding variances. The variances can be used to assign confidence to the identified eigenfrequencies,
6 and effectively eliminate the eigenfrequencies with large variances. This enables a comparison between the
7 identified eigenfrequencies for different ice conditions.

1 Simulated data were used to assess the accuracy of the identified modal parameters during ice-structure
2 interactions, and they were further used to guide the choice of parameters for the subspace identification
3 when applied to measured data. The measured data consisted of 150 recordings of ice actions against the
4 Norströmsgrund lighthouse in the Northern Baltic Sea. The results were sorted into groups defined by the
5 observed ice conditions and governing ice failure mechanisms during the ice-structure interaction. The
6 identified eigenfrequencies varied within each individual group and between the groups. Based on identified
7 modal parameters, we suggested which eigenmodes play an active role in the interaction processes at the ice-
8 structure interface and discussed the possible sources of errors.

1. Introduction

1 The understanding of ice-structure interaction originates from observations and measurements of various ice

*Author for correspondence : Torodd.nord@ntnu.no

†Present address:

Department of Civil and Environmental Engineering, Faculty of
Engineering Science, NTNU, Høgskoleringen 7a, 7491, Trondheim,
Norway

1
2
3
4
5 2 features interacting with structures such as lighthouses, bridge piers and offshore structures. The monitoring
6 3 of structural responses on platforms in Cook Inlet, Alaska began more than 50 years ago (1). It was soon
7 4 discovered that ice forces varied depending on the ice conditions, and therefore, the measurements of the
8 5 structural response were often supplemented with measurements of physical and mechanical properties of the
9 6 ice (2). Despite the measurement complexity and cost, several full-scale monitoring campaigns in (sub-)Arctic
10 7 areas were conducted in the past, many of which involved lighthouse structures (3, 4). Drifting ice against a
11 8 structure may result in various modes of ice-structure interaction. Some of these are violent with ice forces and
12 9 structural responses that represent a threat against the structural integrity, whereas other modes pose no
13 10 concern at all. These modes depend on both the structure and the ice. Structures with sloped walls at the ice-
14 11 structure interface typically promote a flexural type of ice failure, while vertically sided structures typically
15 12 promote crushing failure. Thus, sloped-walled structures are subject to significantly lower ice forces than
16 13 vertically sided structures, but they often incur a higher construction expense (5).

17 14 Ice forces on offshore structures have been debated for decades. Design engineers still find it challenging to
18 15 determine consistent load estimates pertaining to the expected ice conditions. A study by Timco and
19 16 Croasdale (6) demonstrated the difficulties in the year 2006 when they invited international experts to
20 17 calculate the ice forces under some selected scenarios of a structure interacting with first-year level ice, first-
21 18 year ridge and multi-year ice floes. Considerable scatter was presented for the different cases, up to a factor of
22 19 11 between the lowest and highest load estimates for a conical structure subject to level ice. Lighthouses are no
23 20 exception in terms of the challenges faced in the design of offshore structures in ice-infested waters. After
24 21 revisiting 69 lighthouses in the St. Lawrence Waterway, Danys (7) found that many old lighthouses with
25 22 design pressures in the range of 0.55-0.76 MPa were damaged, whereas structures with design pressures in the
26 23 range 2.0-2.8 MPa were undamaged. A few lighthouses in the Baltic Sea, which had design loads in the latter
27 24 range, were also damaged due to ice actions (5). Many of the lighthouses were built with vertical walls at the
28 25 ice-structure interface, allowing a greater risk for structural damage. In particular, narrow structures with a
29 26 low aspect ratio (diameter of the structure at the waterline divided by the ice thickness) were noted to be
30 27 vulnerable to damage, due to excessively low design pressures suggested by the standards (5, 8).

31 28 Consequently, recent guidelines for the design of Arctic offshore structures were modified to account for the
32 29 high ice pressures at low aspect ratios.

33 30 To this end, sensors and measurement techniques were developed to handle the harsh Arctic environment as
34 31 lighthouses and oil platforms were instrumented. The aim was to mitigate ice forces on offshore structures. It
35 32 was soon discovered that the structural integrity was threatened not only by the high ice forces, but also the
36 33 severe ice-induced vibrations (IIV) that followed from the dynamic ice actions (1). IIV represents a threat in
37 34 the form of low-cycle fatigue and illness of people exposed to the vibrations, and in a few cases, it was the
38 35 primary cause of structural damage (1, 4, 9). Although phenomenological models exist to predict IIV, i.e., as

1
2
3
4
5
6
7
8 36 reported in (10, 11), the origin of the vibrations is still under debate (12), and the ice conditions in which IIV
9 37 occurs are still not entirely known. Single events of IIV can also pose a threat to the structural integrity. The
10 38 most critical and famous IIV episode occurred in the Beaufort sea in 1986, when the 90 by 90m wide oil
11 39 platform Molikpaq encountered a multi-year ice floe (13), resulting in liquefaction of the soil foundation. As
12 40 platforms have been deployed in ice-choked waters in regions such as Cook Inlet, Alaska, USA and Bohai Sea,
13 41 China, for decades, their remaining lifetimes decrease, making structural health monitoring (SHM)
14 42 increasingly relevant.

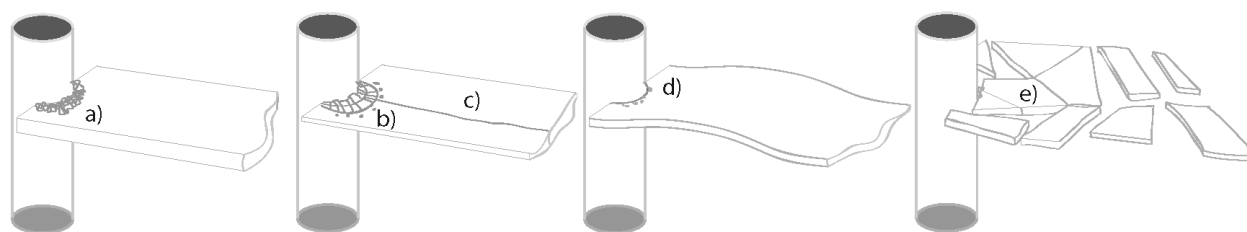
15 43 On the massive Confederation Bridge, monitoring programmes were employed to assessing ice loads and
16 44 SHM (14-16). Simulated damage in conjunction with response measurements under different ambient
17 45 loadings that included ice loads were used to evaluate the possibility for damage detection. On that particular
18 46 structure, ice actions were considered as part of the environmental variability of modal parameters. The
19 47 Confederation bridge is a massive structure, and smaller structures may experience a higher influence of ice
20 48 actions on the modal parameters. A limited number of studies have addressed the changes in modal
21 49 parameters caused by different types of ice conditions and ice failure mechanisms; however, some
22 50 experimental (17, 18) and simulation studies (19) have indicated that added mass and damping may occur. It
23 51 is, thus, unknown to what extent the size of the structure relative to the severity of the ice conditions causes
24 52 system changes, e.g., changes in the eigenfrequency, damping and mode shapes, or the introduction of
25 53 nonlinearities. It is also unknown for which ice conditions the true modal properties can be identified and
26 54 when the underlying assumptions of the applied algorithms are violated the most.

27 55 Even though many arctic offshore structures are located in vulnerable areas where a structural failure may
28 56 have fatal consequences for the environment, it is still unknown whether vibration-based SHM is feasible
29 57 during the ice-covered months. This is relevant not only for hydrocarbon exploitation, but also for advancing
30 58 the development of offshore wind power in cold climates. The null hypothesis is that the feasibility depends
31 59 on the severity of the ice-actions relative to the size of the structure, which was partly exploited in (20). An
32 60 automatic routine was applied to identify eigenfrequencies for data records considering various modes of ice-
33 61 structure interaction occurring on the Norströmsgrund lighthouse. The identified frequencies were spread
34 62 and only few time records rendered similar identified frequencies. The origin of both the bias errors and
35 63 variance errors in the estimated modal parameters when using the covariance-driven reference-based
36 64 stochastic subspace identification routine (SSI-cov/ref) was addressed (21). It was shown how the bias error
37 65 could partly be removed, whereas the variance error could only be estimated. A computationally efficient
38 66 implementation was presented in (22), which is exploited in this study as a means to investigate the variability
39 67 in the identified modal parameters for different ice conditions. The remaining paper is structured as follows:
40 68 section 2 explains some fundamentals of ice-structure interaction and ice forces on vertically-sided structures;
41 69 section 3 presents a summary of the SSI-cov/ref algorithm used to identify the modal parameters; section 4
42 60 *Phil. Trans. R. Soc. A.*

70 presents the identified modal parameters and their uncertainties for simulated cases of ice-structure
71 interaction; section 5 presents the identified modal parameters and the corresponding uncertainties for 150
72 recordings of ice-structure interaction on the Norströmsgrund lighthouse; and finally, the concluding remarks
73 are presented in section 6.

75 2. Modes of ice-structure interaction

76 Several types of ice-structure interactions against vertically sided structures are considered in this study, and
77 they are illustrated in Figure 1. The readers are recommended to refer to (23) for an overview of the mechanics
78 of ice-structure interaction and (24) for descriptions of the observed failure types against the Norströmsgrund
79 lighthouse. Continuous brittle crushing (Figure 1a) is governed by the non-simultaneous occurrence of so-
80 called high-pressure zones across the ice-structure interface. The interaction process ongoing at the ice-
81 structure interface also involves the occurrence of many modifications of the ice material, such as
82 recrystallization and microcrack developments (23, 25). The bending type of flexural failure is often initiated
83 by the development of a circumferential crack followed by radial cracks (Figure 1b). Splitting failures (Figure
84 1c) are usually observed when the interacting ice sheet has a low lateral confinement. The buckling type
85 (Figure 1d) of flexural failure is governed by a build-up of curvature in the ice sheet. Winds and waves as well
86 as ice management can generate fields of broken ice (Figure 1e) that cause small impacts from floes of various
87 sizes onto the walls of the structure. The floes split and pass around the structure, while the wind and wave
88 actions contribute significantly to the total force. The last interaction type considered in this study is creep, in
89 which the ice floe rests against the structure. For simplicity, no distinction is made between limit force, when
90 the driving forces are too low to generate any of the failure mechanisms mentioned above, and limit-stress
91 creep deformation. Among these modes, ice crushing and creep exert the highest forces on the structure. The
92 frequency contents of the ice forces vary substantially not only between the individual failure types but also
93 within the same type of failure with different environmental parameters, see e.g., (20, 26). As ice forces cannot
94 be described as Gaussian white noise, the following sections describe the assessment of the influence of
95 violating the stochastic white-noise input assumption for the SSI-cov/ref.



96
97 Figure 1. Types of failure modes of ice-structure interaction (from Nord et al. (20)).

98

3. Estimation of modal parameters and their uncertainty

(a) System model

Consider the linear time-invariant system described by a discrete time state-space model:

$$\mathbf{x}_{k+1} = \mathbf{A}\mathbf{x}_k + \mathbf{B}\mathbf{u}_k \quad (1)$$

$$\mathbf{y}_k = \mathbf{C}\mathbf{x}_k + \mathbf{D}\mathbf{u}_k + \mathbf{e}_k \quad (2)$$

where $\mathbf{x}_k \in \mathbb{R}^n$ is the state vector, $\mathbf{u}_k \in \mathbb{R}^m$ is the input vector, $\mathbf{y}_k \in \mathbb{R}^r$ is the measurement vector and

$\mathbf{A} \in \mathbb{R}^{n \times n}$, $\mathbf{B} \in \mathbb{R}^{n \times m}$, $\mathbf{C} \in \mathbb{R}^{r \times n}$ and $\mathbf{D} \in \mathbb{R}^{r \times m}$ are the system matrices. Here, n is the model order and r is the number of sensors. The measurements \mathbf{y}_k are corrupted with the measurement error \mathbf{e}_k which is modelled as a white noise random process. The white noise random process is also used to model the input \mathbf{u}_k , which is unknown for many practical applications, and the state-space model is thus reduced to

$$\mathbf{x}_{k+1} = \mathbf{A}\mathbf{x}_k + \mathbf{w}_k \quad (3)$$

$$\mathbf{y}_k = \mathbf{C}\mathbf{x}_k + \mathbf{v}_k \quad (4)$$

where $\mathbf{w}_k = \mathbf{B}\mathbf{u}_k$ and $\mathbf{v}_k = \mathbf{D}\mathbf{u}_k + \mathbf{e}_k$ are the process and output noise, respectively.

We aim to identify matrices \mathbf{A} and \mathbf{C} from which the modal frequencies, damping and mode shapes can be obtained. The eigenvalues and eigenvectors of the system in Eqs. (3) and (4) become

$$(\mathbf{A} - \lambda_i \mathbf{I})\phi_i = 0 \quad (5)$$

$$\phi_i = \mathbf{C}\phi_i \quad (6)$$

from which the continuous time eigenvalues μ , eigenfrequencies f_i and damping coefficients ξ_i (in % of critical) can be obtained as follows:

$$\mu_i = \frac{\ln \lambda_i}{T}, \quad f_i = \frac{|\mu_i|}{2\pi}, \quad \xi_i = -100 \frac{\Re(\mu_i)}{|\mu_i|} \quad (7)$$

where T is the sampling period.

(b) Stochastic subspace identification (SSI) algorithm

In the following two sections, the covariance-driven SSI-cov/ref and the data-driven Unweighted Principal Component (UPC) SSI algorithm are briefly introduced; but for thorough explanations, see (27). Let r be the number of sensors, r_0 be the number of reference sensors, and p and q be the parameters chosen such that

125 $pr \geq qr_0 \geq n$, where n is the model order. The algorithm utilises the output data to build a subspace matrix

126 $H_{p+1,q} \in \mathbb{R}^{(p+1)r \times qr_0}$ which (for a sufficient number of samples) may be decomposed as

$$127 \quad H_{p+1,q} = O_{p+1} Z_q, \quad (8)$$

128 where $O_{p+1} = \begin{bmatrix} C^T & (CA)^T & \cdots & (CA^p)^T \end{bmatrix}^T$ is the observability matrix and matrix Z_q depends on the chosen

129 subspace identification algorithm. The observability matrix O_{p+1} is constructed from a singular value

130 decomposition (SVD) of the subspace matrix $H_{p+1,q}$, which is further truncated at a user-defined model order

131 n :

$$132 \quad H_{p+1,q} = \begin{bmatrix} U_1 & U_0 \end{bmatrix} \begin{bmatrix} \Sigma_1 & 0 \\ 0 & \Sigma_0 \end{bmatrix} \begin{bmatrix} V_1^T \\ V_0^T \end{bmatrix}, \quad (9)$$

$$133 \quad O_{p+1} = U_1 \Sigma_1^{1/2}. \quad (10)$$

134 The C matrix can be directly extracted from the first block of r rows of the observability matrix O_{p+1} , while

135 the A matrix can be obtained from a least squares solution of

$$136 \quad O_{p+1}^\uparrow A = O_{p+1}^\downarrow, \quad (11)$$

137 where

$$138 \quad O_{p+1}^\uparrow = \begin{bmatrix} C \\ CA \\ \vdots \\ CA^{p-1} \end{bmatrix}, \quad O_{p+1}^\downarrow = \begin{bmatrix} CA \\ CA^2 \\ \vdots \\ CA^p \end{bmatrix}.$$

140 (c) Estimate of the subspace matrix

141 "Future" and "past" output data matrices are assembled from a total number of $N + p + q$ samples as follows:

$$142 \quad Y^+ = \begin{bmatrix} Y_{q+1} & Y_{q+2} & \cdots & Y_{N+q} \\ Y_{q+2} & Y_{q+3} & \cdots & Y_{N+q+1} \\ \vdots & \vdots & \ddots & \vdots \\ Y_{q+p+1} & Y_{q+p+2} & \cdots & Y_{N+q+p} \end{bmatrix}, \quad Y^- = \begin{bmatrix} Y_q^{(\text{ref})} & Y_{q+1}^{(\text{ref})} & \cdots & Y_{N+q-1}^{(\text{ref})} \\ Y_{q-1}^{(\text{ref})} & Y_q^{(\text{ref})} & \cdots & Y_{N+q-2}^{(\text{ref})} \\ \vdots & \vdots & \ddots & \vdots \\ Y_1^{(\text{ref})} & Y_2^{(\text{ref})} & \cdots & Y_N^{(\text{ref})} \end{bmatrix} \quad (12)$$

143 where $Y_k^{(\text{ref})} \in \mathbb{R}^{r_0}$ contains the reference sensor data. These data matrices are further normalised with respect

144 to their numbers of columns, such that

$$145 \quad \tilde{Y}^+ = \frac{1}{\sqrt{N}} Y^+, \quad \tilde{Y}^- = \frac{1}{\sqrt{N}} Y^-. \quad (13)$$

146 From the data matrices, the covariance-driven subspace matrix is defined:

$$147 \quad \tilde{H}^{\text{cov}} = \tilde{Y}^+ (\tilde{Y}^-)^T, \quad (14)$$

148 while in the data-driven case, the subspace matrix is defined:

$$149 \quad \tilde{H}^{\text{dat}} = \tilde{Y}^+ (\tilde{Y}^-)^T (\tilde{Y}^- (\tilde{Y}^-)^T)^{\dagger} \tilde{Y}^-. \quad (15)$$

150 Alternatively, the data-driven subspace matrix can be estimated from the thin LQ decomposition:

$$151 \quad \begin{bmatrix} \tilde{Y}^- \\ \tilde{Y}^+ \end{bmatrix} = \begin{bmatrix} R_{11} & 0 \\ R_{21} & R_{22} \end{bmatrix} \begin{bmatrix} Q_1 \\ Q_2 \end{bmatrix} \quad (16)$$

152 from which $\tilde{H}^{\text{dat}} = R_{21} Q_1$, where $R_{21} \in \mathbb{R}^{(p+1)r \times q_0}$ and $Q_1 \in \mathbb{R}^{q_0 \times N}$. Note that because of the orthogonal
153 properties of Q_1 , the observability matrix is estimated directly from R_{21} in the implementation.

154 (d) Covariance estimate of the subspace matrix

155 Statistical uncertainty in the identified modal parameters may occur due to e.g. non-white excitation of the
156 system, a finite number of data samples, non-stationarity etc., which leads to variance errors in the modal
157 parameters. In what follows, the covariance computation of the modal parameters is based upon an
158 underlying covariance-driven SSI algorithm and propagation of first-order perturbations from the data to the
159 modal parameters (21). Full-scale validations of the method were presented in (28), while our study applies a
160 computationally efficient implementation (22). Reviews of existing methods for covariance estimation of
161 identified modal parameters are presented in (28) and (29).

162 In the covariance-driven SSI, the covariance of the subspace matrix were calculated by first splitting \tilde{Y}^+ and
163 \tilde{Y}^- into n_b blocks

$$164 \quad \tilde{Y}^+ = \frac{\sqrt{N}}{\sqrt{N_b}} [\tilde{Y}_1^+ \quad \dots \quad \tilde{Y}_{n_b}^+], \quad \tilde{Y}^- = \frac{\sqrt{N}}{\sqrt{N_b}} [\tilde{Y}_1^- \quad \dots \quad \tilde{Y}_{n_b}^-], \quad (17)$$

165 where for simplicity, $N_b \cdot n_b = N$; subsequently, the blocks were normalised according to the block length.

166 From each data block in Eq. (17), the subspace matrix estimate \tilde{H}_j^{cov} is built with

$$167 \quad \tilde{H}_j^{\text{cov}} = \tilde{Y}_j^+ (\tilde{Y}_j^-)^T \quad (18)$$

168 , and its covariance estimate $\hat{\Sigma}_{\tilde{H}^{\text{cov}}}$ reads as

$$169 \quad \hat{\Sigma}_{\tilde{H}^{\text{cov}}} = \frac{N}{n_b(n_b-1)} \sum_{j=1}^{n_b} (\text{vec}(\tilde{H}_j^{\text{cov}}) - \text{vec}(\tilde{H}^{\text{cov}})) (\text{vec}(\tilde{H}_j^{\text{cov}}) - \text{vec}(\tilde{H}^{\text{cov}}))^T. \quad (19)$$

170 (e) Covariance estimate of the modal parameters

171 The principle of the method is to propagate the covariance of the subspace matrix, Σ_H , to the modal
 172 parameters through first-order perturbations. First-order perturbations of the subspace matrix H are first
 173 propagated to the system matrices A and C as follows:

$$174 \begin{bmatrix} \text{vec}(\Delta A) \\ \text{vec}(\Delta C) \end{bmatrix} = J_{AC,H} \text{vec}(\Delta H) \quad (20)$$

175 where $J_{AC,H}$ is the sensitivity matrix according to the definitions given in (21, 28) and (30). The covariance of
 176 the vectorised system matrices, $\Sigma_{A,C}$, can be defined as,

$$177 \Sigma_{A,C} \stackrel{\text{def}}{=} \text{cov} \left(\begin{bmatrix} \text{vec}(\Delta A) \\ \text{vec}(\Delta C) \end{bmatrix} \right) = J_{AC,H} \Sigma_H J_{AC,H}^T, \quad (21)$$

178 in which the covariance of the subspace matrix, Σ_H , can be estimated by dividing the subspace matrix into
 179 blocks as described in the previous section and in (22). The perturbations of the modal parameters can be
 180 described as functions of the vectorised system matrices as follows:

$$181 \Delta f_i = J_{f_i,A} \text{vec}(\Delta A), \quad \Delta \xi_i = J_{\xi_i,A} \text{vec}(\Delta A), \quad \Delta \varphi_i = J_{\varphi_i,AC} \begin{bmatrix} \text{vec}(\Delta A) \\ \text{vec}(\Delta C) \end{bmatrix} \quad (22)$$

182 where the sensitivities $J_{f_i,A}$, $J_{\xi_i,A}$, and $J_{\varphi_i,AC}$ are defined per mode i . Finally, the covariances of the modal
 183 parameters are obtained as:

$$184 \text{cov} \left(\begin{bmatrix} f_i \\ \xi_i \end{bmatrix}, \begin{bmatrix} f_j \\ \xi_j \end{bmatrix} \right) = \begin{bmatrix} J_{f_i,A} & 0_{1,m} \\ J_{\xi_i,A} & 0_{1,m} \end{bmatrix} \Sigma_{AC} \begin{bmatrix} J_{f_j,A} & 0_{1,m} \\ J_{\xi_j,A} & 0_{1,m} \end{bmatrix}^T \quad (23)$$

$$185 \text{cov} \left(\begin{bmatrix} \Re(\varphi_i) \\ \Im(\varphi_i) \end{bmatrix}, \begin{bmatrix} \Re(\varphi_j) \\ \Im(\varphi_j) \end{bmatrix} \right) = \begin{bmatrix} \Re(J_{\varphi_i,AC}) \\ \Im(J_{\varphi_i,AC}) \end{bmatrix} \Sigma_{AC} \begin{bmatrix} \Re(J_{\varphi_j,AC}) \\ \Im(J_{\varphi_j,AC}) \end{bmatrix}^T.$$

186 In this study, the implementation is performed in accordance with algorithm 4 presented in (22) which yields
 187 fast computations when multiple model orders are considered.

189 4. Modal parameter identification using simulated data of dynamic ice-structure 190 interactions

191 Since ice forces have been measured by means of both inverse techniques and installations of force panels at
 192 the ice-structure interface, some knowledge exists concerning their appearance in time and frequency
 193 domains. The continuous brittle crushing process, which is one of the interaction types decisive for design
 194 loads, is described as a random process (31). Nonsimultaneous contact across the interface between the

1
2
3
4
5
6
7
8 195 structure that changes in space and time causes local pressures to vary across the interface (32). This means
9 196 that the force varies randomly superimposed to a mean level. The structure, in some cases, slows down the
10 197 drifting ice floe(s), thereby influences the driving force(s); therefore, the mean level is seldom constant. The
11 198 slow-varying processes of ice forces are also influenced by uneven ice thickness, stochastic variation of ice
12 199 strength, and delayed elastic and viscous properties of the ice, in addition to the intermittent occurrences of
13 200 other failure processes; all of these may contribute to a non-white forcing onto the structure.
14 201 In this study, a phenomenological ice-structure interaction model (19, 33) is used to investigate the effect of
15 202 variation in ice conditions on the identified modal parameters and their uncertainties. A MATLAB
16 203 implementation of the model, including a single-degree-of-freedom structural representation in the modal
17 204 domain, is available from Mendeley data (34). The ice model is coupled to the modal characteristics of the
18 205 Norströmsgrund lighthouse, extracted from the finite element software Abaqus CAE.
19 206 The Norströmsgrund lighthouse (Figure 2) is a gravity-based concrete structure located in the Gulf of Bothnia,
20 207 Sweden. The lighthouse was constructed in 1971 and designed to withstand ice loads of 2.2 MN/m. Below the
21 208 mean water level, the main structure and foundation caisson are filled with sand. Eight concrete bulkheads
22 209 stiffen the foundation frame, and a 0.7 m thick concrete foundation plate rests on a top layer of cement-
23 210 grouted crushed stones and a lower layer of morainic soil. The wall thickness varies between 0.2 m at the top
24 211 and 1.4 m at the mean water level. Service personnel visiting Norströmsgrund late in the winter of 1972
25 212 observed heavy vibrations due to ice actions. In 1973, thin cracks were detected in the most strained area of
26 213 the superstructure walls close to the ground floor. Despite that the cracks pervaded through the wall and
27 214 moisture intrusion was observed, it was concluded that the structural integrity remained intact (9).
28 215 The finite element model, modelled with quadrilateral finite membrane-strain shell elements with reduced
29 216 integration (S4R) is displayed in Figure 2 and Figure 3. The structural dimensions and material properties are
30 217 obtained from (35) and an elaborate description of the model can be found in (26). Because the structure is
31 218 near axisymmetric, structural modes occur in pairs with almost identical frequencies. Mode shape 1 (and 2) is
32 219 governed by tilt of both the foundation caisson and tower substructure (tower below + 16.5 m) while the
33 220 superstructure deflects in the tilt direction. For mode shape 3 (4), both the tower caisson and tower
34 221 substructure displaces in the opposite direction to the superstructure deflection. Mode shape 5 (6) has the
35 222 same tilt of both the caisson and tower substructure as for mode shape 1, whereas the superstructure deflects
36 223 in opposite direction to the substructure tilt direction. In mode shape 7 (8), the foundation caisson tilts in the
37 224 opposite direction to the tower substructure.



Figure 2. Illustration, picture and finite element model of the Norströmsgrund lighthouse, from Nord et al. (26).

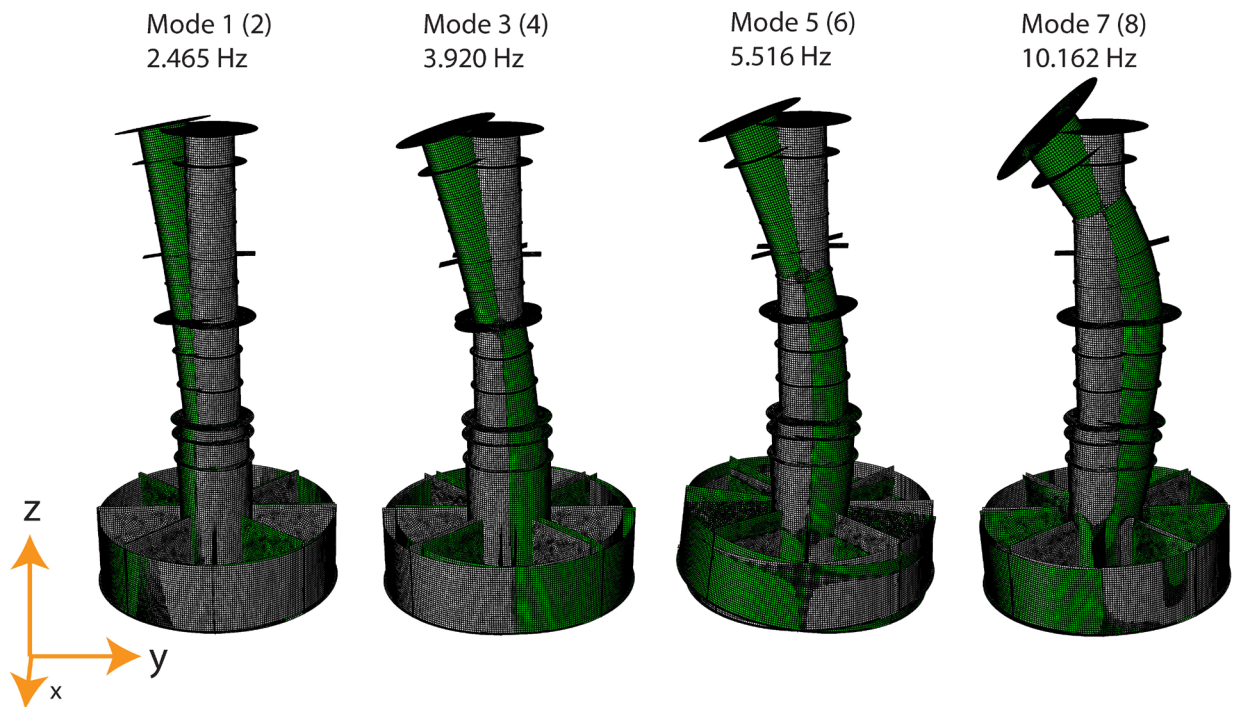


Figure 3. Mode shapes and corresponding natural frequencies of the finite element model (From Nord et al. (26)).

The forces are treated as concentrated loads acting on a linear time-invariant structure that is represented by selected vibration eigenmodes:

$$\ddot{\mathbf{z}}(t) + \mathbf{\Gamma}\dot{\mathbf{z}}(t) + \mathbf{\Omega}^2\mathbf{z}(t) = \mathbf{\Phi}^T\mathbf{S}_p\mathbf{p}(\mathbf{z}, \dot{\mathbf{z}}, t) \quad (24)$$

236 Here, $\mathbf{z}(t) \in \mathbb{R}^{n_m}$ is the vector of modal coordinates, and $n_m = 24$ is the number of eigenmodes used to
 237 assemble the model. The ice force, $\mathbf{p}(\mathbf{z}, \dot{\mathbf{z}}, t) \in \mathbb{R}^{n_p}$, is specified to act on the desired location “Force N-S” in
 238 Figure 2 through the force influence matrix $\mathbf{S}_p \in \mathbb{R}^{n_{\text{DOF}} \times n_p}$, where n_p is the number of force time histories and
 239 n_{DOF} is the number of degrees of freedom.

240 $\mathbf{\Gamma} \in \mathbb{R}^{n_m \times n_m}$ is the diagonal damping matrix populated on the diagonal with the terms $2\xi_j\omega_j$, where ω_j and
 241 ξ_j represent the natural frequency in radians per second and damping ratio corresponding to eigenmode j ,
 242 respectively. $\mathbf{\Omega} \in \mathbb{R}^{n_m \times n_m}$ is a diagonal matrix containing the natural frequencies ω_j , and $\mathbf{\Phi} \in \mathbb{R}^{n_{\text{DOF}} \times n_m}$ is a matrix
 243 collecting the mass-normalised mode shapes. Rayleigh damping is assigned to the model with 2% in modes 1
 244 and 2, increasing up to 20% in mode 24. The lowest four eigenfrequencies and corresponding damping ratios
 245 of the finite element model are given in Table 1, with the corresponding mode shapes displayed in Figure 3.
 246 The axisymmetry of the model leads to mode pairs in the orthogonal directions, with each pair assigned
 247 identical damping values.

248 Table 1. Modal properties of simulation model.

	Mode 1 (2)	Mode 3 (4)	Mode 5 (6)	Mode 7 (8)
f_i [Hz]	2.465	3.920	5.516	10.162
ξ_i [%]	2.000	2.005	2.367	3.642

249 Two time series, each of 600s, were simulated using the ice model. The mean ice thickness and ice velocity
 250 were assumed to be 1 m and 0.1 ms^{-1} , respectively. Time-dependent parameters in the ice model were used to
 251 generate time series with different ice conditions, herein categorised as *slow-varying* and *fast-varying* ice
 252 conditions (Figure 4). Though the ice model is in essence non-linear and dependent on the structural motion,
 253 the non-linearity is considered insignificant at the high ice velocities considered in this work. Under these
 254 conditions, the time between contact and failure of a single ice element is short and consequently the motion
 255 of the structure is insignificant compared to the deformation of the ice element. At low ice drift velocities
 256 strongly non-linear interactions commonly referred to as intermittent crushing and frequency lock-in, become
 257 prevalent and the presented approach is no longer applicable.

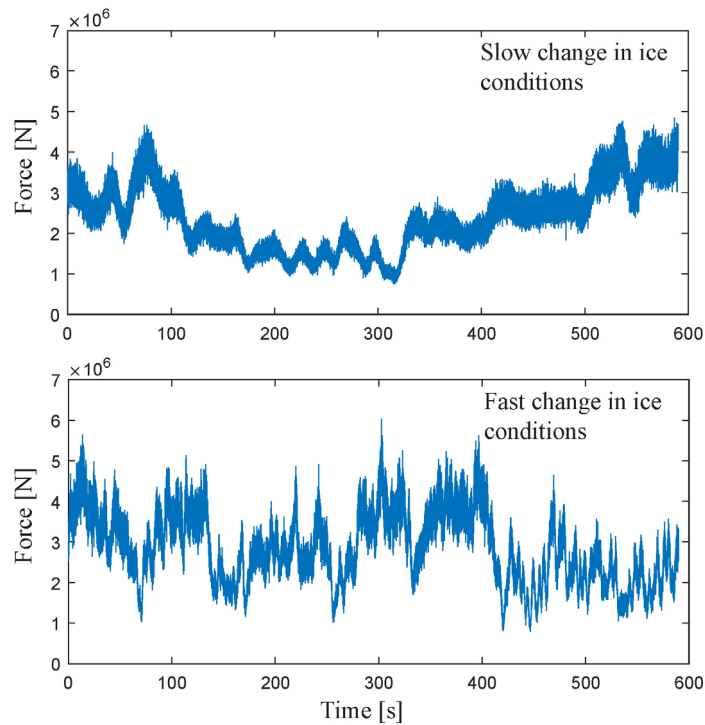


Figure 4. Simulated force time histories during interaction with slow-varying (top figure) and fast-varying (bottom) ice conditions.

Four measurements of accelerations extracted at locations specified in Figure 2 were used for the subspace identification (SSI-cov/ref), and throughout the paper the number of reference sensors is set equal to the total number of sensors $r = r_0 = 4$. This involved the same number of sensors with the same locations as installed on the lighthouse in the winters of years 2001 to 2003.

For comparison, a white noise force with an amplitude $0.3294 \cdot 10^6$ N was applied to the same model and with accelerations extracted at the same locations as for the ice-structure interaction simulations. In the simulations, the system matrices A, B, C, D in Eqs. (1) and (2) were assembled from the same modally reduced order finite element model as described above, with forces acting in the same nodes and the sensors located at the same nodes. Section 2.1 in (26) describes in depth how the modal properties of the structure are used to assemble the system matrices A, B, C, D .

Recordings of 59000 sample points were added 5 % Gaussian white noise. The sampling frequency was 100 Hz, the number of blockrows was set as 100 and the number of blocks for the covariance of the subspace matrix, n_b , was set as 60.

277 Tolerance deviances to frequency, damping and MAC values, as well as the normalised standard deviation of
 278 the frequency, $\frac{\hat{\sigma}_{\omega_i}}{\omega_i}$ were added into the stabilization diagram. A pole at order n was considered stable if the
 279 deviances in frequency, damping, MAC, and normalised standard deviation of the frequency between a pole
 280 at order n and $n-1$ were less than or equal to 0.01, 0.05, 0.95 and 0.05, respectively. A routine was used to
 281 pick eigenmodes automatically from the stabilization diagrams. The poles were first sorted with increasing
 282 corresponding absolute values, and a user-defined frequency slack value, S_f , defined the range from which
 283 the poles were collected. From the eigenvectors of the poles in that range, MAC values were calculated
 284 between all eigenvectors, and a reference eigenmode was selected as the pole that rendered the highest sum of
 285 MAC values. The MAC values between the reference eigenmode and the eigenvectors of the remaining poles
 286 in that frequency range (defined by S_f) must lie within a user-defined MAC-slack, S_{MAC} to be further
 287 considered. The third acceptance criterion checked whether the poles that fulfilled the MAC-slack also
 288 fulfilled a damping slack, S_ζ . Finally, the selected eigenmode contained the mean values of the frequency,
 289 damping, mode shape and their corresponding variances. S_f , S_ζ and S_{MAC} were chosen to be 0.02, 0.3 and
 290 0.5, respectively.

291 The stabilization diagrams in Figure 5 show the first four identified eigenmodes, with the square root of the
 292 identified variance (standard deviation), $\pm\hat{\sigma}_\omega$, added to each pole in the diagram. Both the slow and fast-
 293 varying ice conditions rendered clear columns of stable poles, and the differences were noticeable mainly in
 294 the variance estimates. Table 2 presents the automatically selected eigenmodes' frequency, damping and
 295 corresponding standard deviations alongside with the absolute error between the identified and model
 296 frequencies. The results obtained from the time series of ice-structure interaction were compared with the
 297 results obtained from the time series with Gaussian white noise as the input. As expected, the Gaussian white
 298 noise input yielded more accurate frequency estimates than both the ice-structure interaction scenarios, while
 299 the fast-varying ice conditions appeared to render damping as accurate as in the case of the Gaussian white
 300 noise.

302 Table 2. Identified modal parameters (using SSI-cov/ref), standard deviations and absolute errors.

Identified eigenmodes	White noise	Slow-varying ice conditions	Fast-varying ice conditions
	$f_i \pm \hat{\sigma}_{f_i}(\text{Hz}) / (\text{error}(\text{Hz}))$	$f_i \pm \hat{\sigma}_{f_i}(\text{Hz}) / (\text{error}(\text{Hz}))$	$f_i \pm \hat{\sigma}_{f_i}(\text{Hz}) / (\text{error}(\text{Hz}))$

Phil. Trans. R. Soc. A.

Mode 1	$2.465 \pm 0.004 / (0.000)$	$2.454 \pm 0.005 / (0.011)$	$2.462 \pm 0.005 / (0.003)$
Mode 2	$3.923 \pm 0.010 / (0.003)$	$3.925 \pm 0.027 / (0.005)$	$3.909 \pm 0.021 / (0.011)$
Mode 3	$5.517 \pm 0.051 / (0.001)$	$5.527 \pm 0.057 / (0.011)$	$5.505 \pm 0.068 / (0.011)$
Mode 4	$10.148 \pm 0.134 / (0.014)$	$10.173 \pm 0.121 / (0.011)$	$10.140 \pm 0.072 / (0.022)$
	White noise	Slow-varying ice conditions	Fast-varying ice conditions
	$\xi_i \pm \hat{\sigma}_{\xi_i} (\%) / (error \%)$	$\xi_i \pm \hat{\sigma}_{\xi_i} (\%) / (error \%)$	$\xi_i \pm \hat{\sigma}_{\xi_i} (\%) / (error \%)$
Mode 1	$2.149 \pm 0.193 / (0.149)$	$1.627 \pm 0.215 / (0.373)$	$1.804 \pm 0.211 / (0.196)$
Mode 2	$1.793 \pm 0.266 / (0.212)$	$2.239 \pm 0.653 / (0.391)$	$2.070 \pm 0.619 / (0.065)$
Mode 3	$2.623 \pm 0.726 / (0.256)$	$2.092 \pm 0.837 / (0.275)$	$2.188 \pm 0.867 / (0.178)$
Mode 4	$3.840 \pm 0.961 / (0.198)$	$3.438 \pm 0.975 / (0.204)$	$3.566 \pm 0.635 / (0.075)$

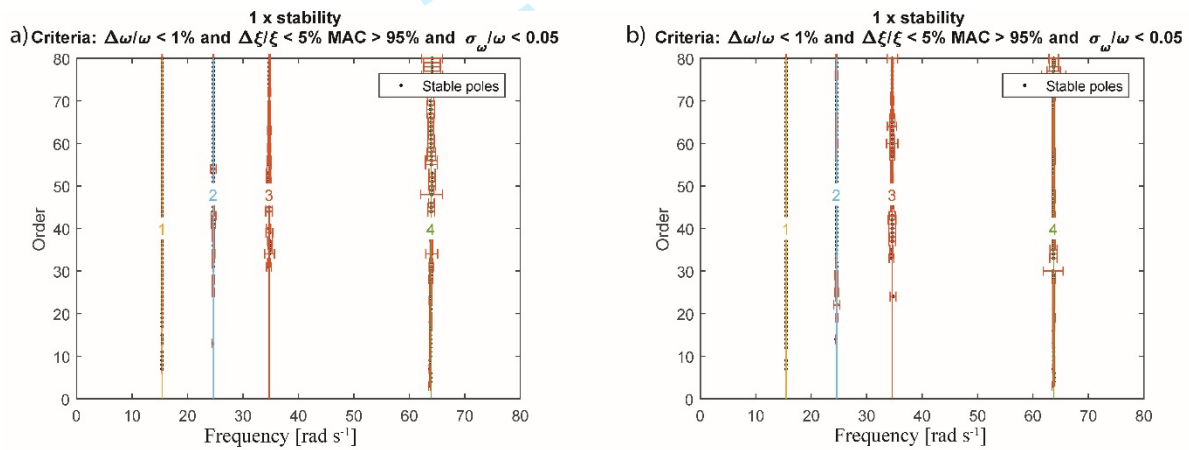


Figure 5. Stabilization diagrams for a) slow-varying ice conditions b) fast-varying ice conditions.

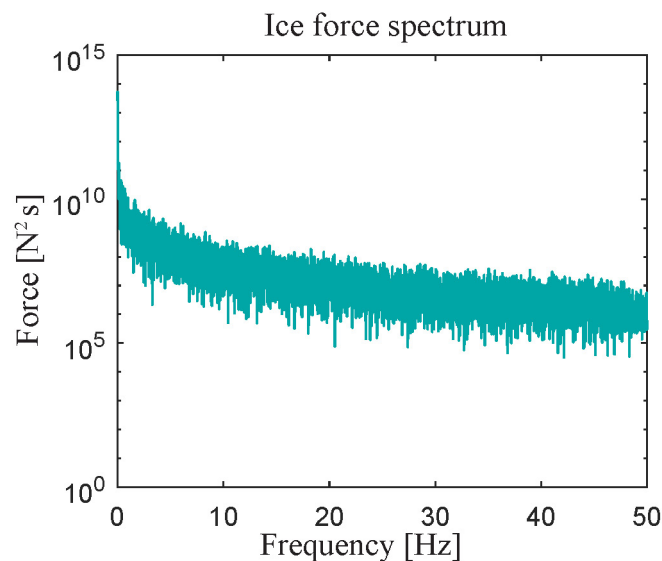
Since simulations with the ice model were computationally expensive, it was not feasible to check whether the point estimate of variances of the identified frequency and damping coincided with the sample statistics for multiple simulations. Instead, sample statistics were generated using Monte Carlo simulations as follows:

Continuous brittle crushing ice forces, $p_{i,m}(t)$, were generated by realization of a typical ice force spectrum from the Norströmsgrund lighthouse, $\Lambda_{pi}(\omega)$, which was discretised using $\Delta\omega = 0.01 \text{ rad s}^{-1}$:

$$p_{i,m}(t) = \sqrt{2\Delta\omega} \operatorname{Re} \left(\sum_{k=1}^N \sqrt{\Lambda_{pi}(\omega_k)} e^{i(\omega_k t + \alpha_{ik})} \right), \quad (25)$$

where α_{ik} is the phase angle modelled as uniformly random between 0 and 2π .

314 The ice forces were first obtained with a sampling frequency of 1660 Hz and further resampled down to 100
 315 Hz (Figure 6). The simulated acceleration time series was thereafter generated by using Eqs. (1) and (2) by
 316 applying the ice force $p_{i,m}(t)$ onto the ice-action point (cf. Figure 2). In the simulations, the system matrices
 317 A, B, C, D were assembled from the same modally reduced order finite element model as described
 318 previously. In total 250 acceleration time series were simulated using ice forces.



319
 320 Figure 6. Ice force spectrum used for monte-carlo simulations.

321 Five percent Gaussian white measurement noise was added to the four acceleration signals, and all the
 322 settings for the SSI-cov/ref were identical to those in the abovementioned examples. For each identification,
 323 the first automatically identified eigenmodes in the frequency range 0-12 Hz with their corresponding
 324 damping and variances were stored. For the sake of further illustrations and result presentation, the standard
 325 deviations were calculated from the variances. 250 simulated time series with Gaussian white noise input with
 326 an amplitude of $0.3294 \cdot 10^6$ N was used for comparison. The collection of identified frequencies during the
 327 ice-structure interactions shows presence of spurious modes, spread out from the true eigenfrequency, most
 328 with larger standard deviations (Figure 7). For simulations of ice-structure interactions, the sample standard
 329 deviations for the identified frequencies and damping (σ_{f_i} and σ_{ξ_i}) did not correspond to the mean values of
 330 the identified standard deviations ($\hat{\sigma}_{f_i}$ and $\hat{\sigma}_{\xi_i}$, Table 3), a result which is significantly influenced by four
 331 spurious frequencies below 2 Hz (Figure 7a). In the case of the simulations with Gaussian white noise, the
 332 sample standard deviations corresponded well with the identified standard deviations.

334 Table 3. Natural frequencies and damping ratios of the first identified eigenmode. μ_{f_i} and μ_{ξ_i} : mean values
 335 over 250 simulations. $\hat{\sigma}_{f_i}$ and $\hat{\sigma}_{\xi_i}$: mean of the estimated standard deviations. σ_{f_i} and σ_{ξ_i} : sample standard
 336 deviation.

Mode	μ_{f_i} (Hz)	$\hat{\sigma}_{f_i}$	σ_{f_i}	μ_{ξ_i} (%)	$\hat{\sigma}_{\xi_i}$	σ_{ξ_i}
Mode 1 (ice-structure interaction)	2.459	$1.153 \cdot 10^{-2}$	$1.202 \cdot 10^{-1}$	1.530	$8.096 \cdot 10^{-1}$	$4.288 \cdot 10^{-1}$
Mode 1 (white noise input)	2.465	$4.999 \cdot 10^{-3}$	$4.857 \cdot 10^{-3}$	2.047	$2.152 \cdot 10^{-1}$	$1.977 \cdot 10^{-1}$
Mode 1 (ice-structure interaction) Short time series	2.433	$2.317 \cdot 10^{-2}$	$5.887 \cdot 10^{-2}$	1.859	1.864	$4.035 \cdot 10^{-1}$
Mode 1 (white noise input) Short time series	2.464	$1.598 \cdot 10^{-2}$	$4.577 \cdot 10^{-3}$	2.004	$7.992 \cdot 10^{-1}$	$1.977 \cdot 10^{-1}$

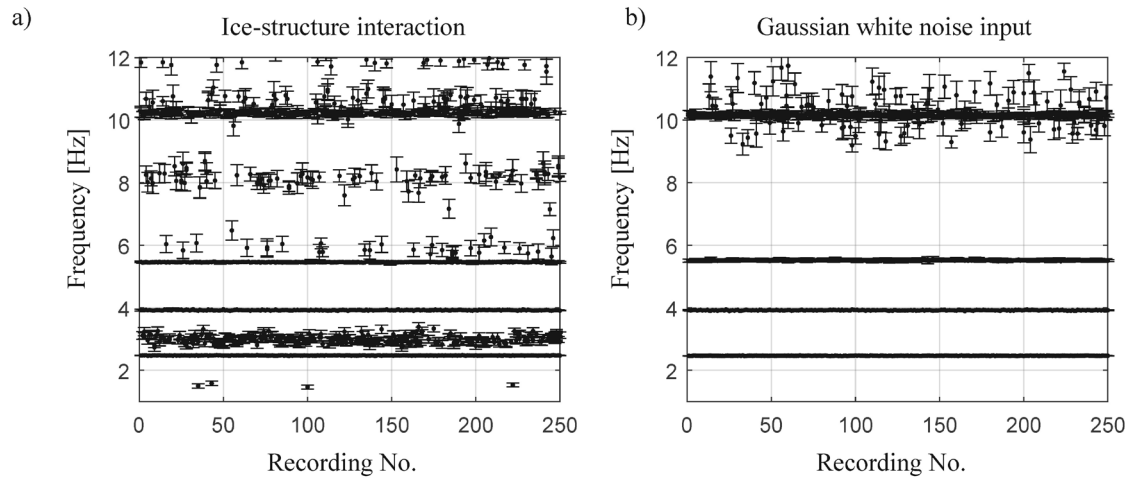


Figure 7. Identified frequencies and their uncertainties for each simulation with a) ice-structure interaction, and b) Gaussian white noise input. Each simulation contained $N=59000$ sample points.

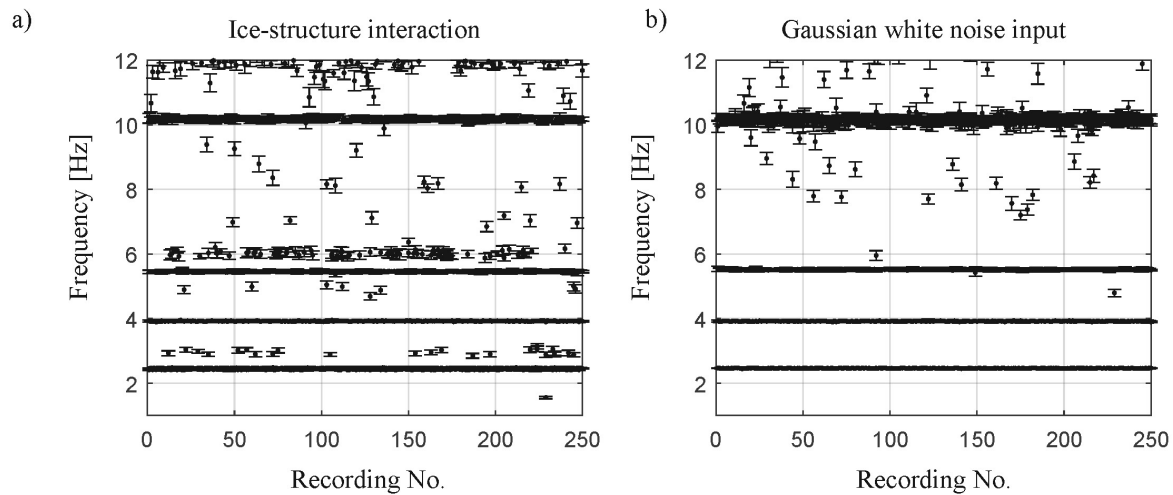
Until now, the simulated time series had a long duration. In the following section, we describe the analysis of the effects of having a short duration of time series and of resampling down to 30 Hz. The short duration resembles the nature of rapidly changing ice conditions, which vary by site. Because we aim to assess the identification of modal parameters for different ice conditions, the duration constraint is inevitable. Figure 7 shows that the variances of the identified frequencies for spurious modes were larger than those for the true eigenmodes; therefore, a tolerance value of the normalised standard deviation that could eliminate spurious modes and retain true eigenmodes was attempted to be determined. Each simulation had 17800 sample points and 5 % noise was added to each acceleration signal. The number of blockrows, number of blocks for the

calculation of the variance of the subspace matrix, n_b , and tolerance value for the stabilization criterion, $\frac{\hat{\sigma}_{\omega_i}}{\omega_i}$, were changed to 30, 20 and 0.03, respectively. All other settings remained as described above. Figure 8 displays the identified eigenfrequencies and their estimated standard deviations for both simulations with ice-structure interaction and Gaussian white noise input. It was noted that some spurious modes remained in the identifications, some of them with standard deviations in frequency nearly as low as the standard deviations

of true eigenfrequencies. Therefore, reducing the tolerance value, $\frac{\hat{\sigma}_{\omega_i}}{\omega_i}$, further suppressed the correctly

identified eigenfrequencies alongside the spurious frequencies. The eigenfrequencies were reasonably well identified during ice-structure interaction, whereas the ensemble statistics in Table 3 (bottom two rows) show that neither the identified damping nor the mean of the estimated standard deviations, $\hat{\sigma}_{f_i}$ and $\hat{\sigma}_{\xi_i}$ matched

358 with the sample standard deviations σ_{f_i} and σ_{ξ_i} . These discrepancies may be explained by both the violation
 359 of stationary white noise excitation and the chosen slack values for the automatic mode selection routine.

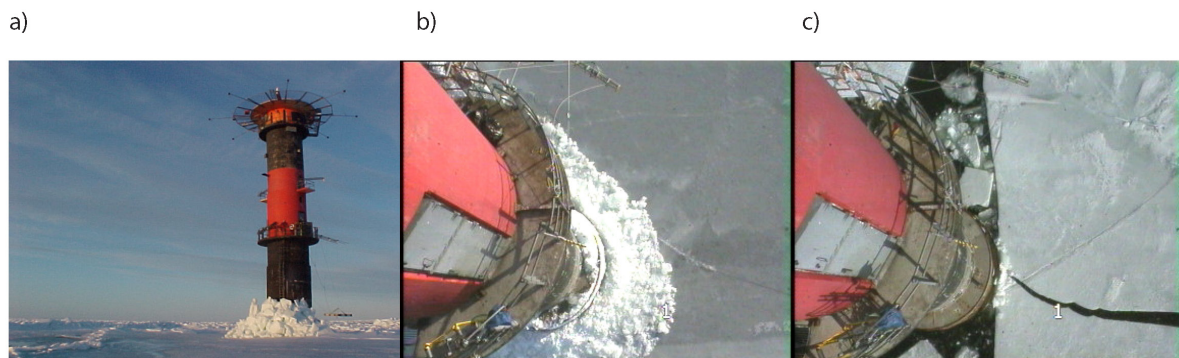


362 Figure 8. Identified frequencies and their uncertainties for each simulation with a) ice-structure interaction,
 363 and b) Gaussian white noise input. Each simulation contained $N=17800$ sample points.

365 5. Modal parameter identification using measured data of ice-structure interactions

366 (a) Measurements of ice-structure interaction at Norströmsgrund lighthouse

367 At the Norströmsgrund lighthouse (Figure 9), the structural responses, ice forces, ice thicknesses, air
 368 temperatures, wind speeds, wind directions and ice conditions during the winter seasons from 1999 to 2003
 369 were monitored in the measurement projects LOLEIF (LOw LEvel Ice Forces) (36) and STRICE (STRuctures in
 370 ICE) (24). Nine panels were installed at the mean water level to measure the ice forces (36), covering the outer
 371 perimeter from 0 (North) to 162 degrees. Four acceleration channels (Shaevitz SB) and four inclinometer
 372 channels (Schaevitz DC inclinometer series and Applied Geomechanics biaxial Model 716-2A) measured the
 373 structural accelerations in the north-south and east-west directions, and the tilts about the same directions,
 374 respectively. The accelerometers were located close to the ice-action point at an elevation of +16.5 m and close
 375 to the top at an elevation of +37.1 m. A summary of the STRICE project and earlier measurement campaigns
 376 can be found in Bjerkås (37).



377
378 Figure 9. The Norströmsgrund lighthouse during ice action: a) rubble formation after ice interaction (Photo by
379 courtesy of Basile Bonnemaire); b) crushing ice failure and c) splitting ice failure.

381 (b) Data selection

382 Extensive efforts were devoted to the selection of data for this study, as several criteria were required to be
383 fulfilled; a similar selection was used in (20), although minor modifications were adopted in the present study.
384 The sampling frequency had a minimum value of 30 Hz, video footage was available to define the type of
385 failure, and the ice failure was governed by one of the aforementioned failure modes for a minimum of 10
386 minutes. The individual data files contained time series of various lengths, and they were selected by
387 operators to capture specific types of interactions. Often, one data file had several events of interaction that
388 fulfilled the criteria above, and each of these events is hereon referred to as a recording. In total, 150
389 recordings with lengths of 10 minutes were selected and further used in this study; of these, the number of
390 recordings pertaining to continuous crushing, flexural, splitting, ice floe, and creep failures were 79, 30, 14, 8
391 and 19, respectively. Examples of acceleration signals during continuous crushing and flexural failures are
392 displayed in Figure 10. For these examples, the continuous crushing excites the modes with lower
393 eigenfrequencies stronger than the flexural failure does (Figures 10 b and d). An important disadvantage with
394 the STRICE dataset was that data were stored with different sampling frequencies depending on the level of
395 dynamic response of the lighthouse. If the vibrations were significant, the original data was resampled down
396 and stored at 100 Hz, whereas if less dynamic ice action was present, data was resampled and stored at 30 Hz.
397 For the purpose of this study, regardless of which sampling frequency the data were stored at, all
398 accelerations were resampled to 30 Hz.

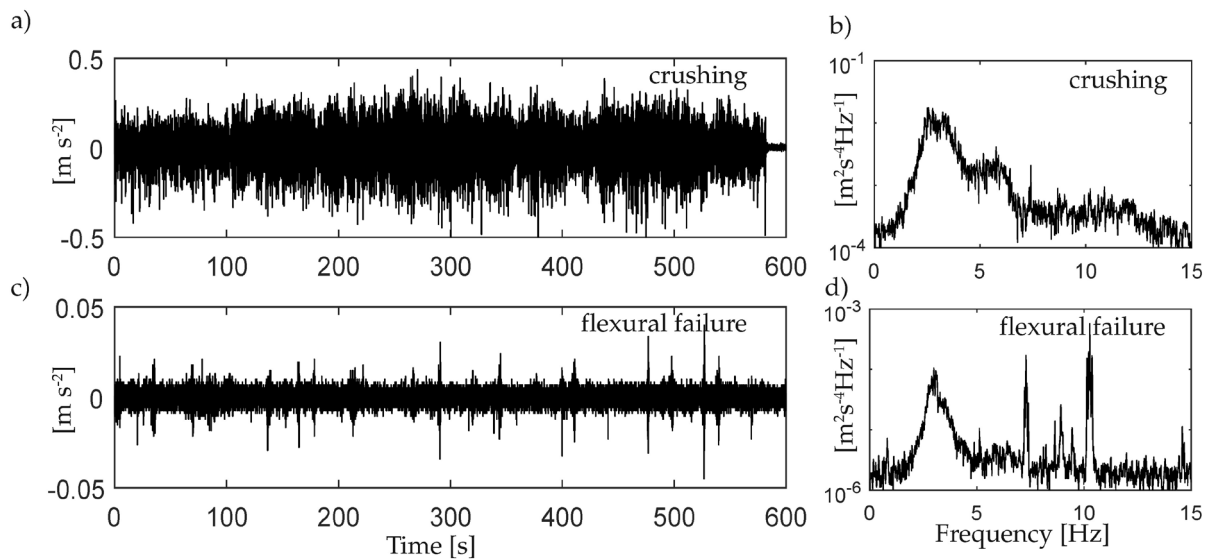
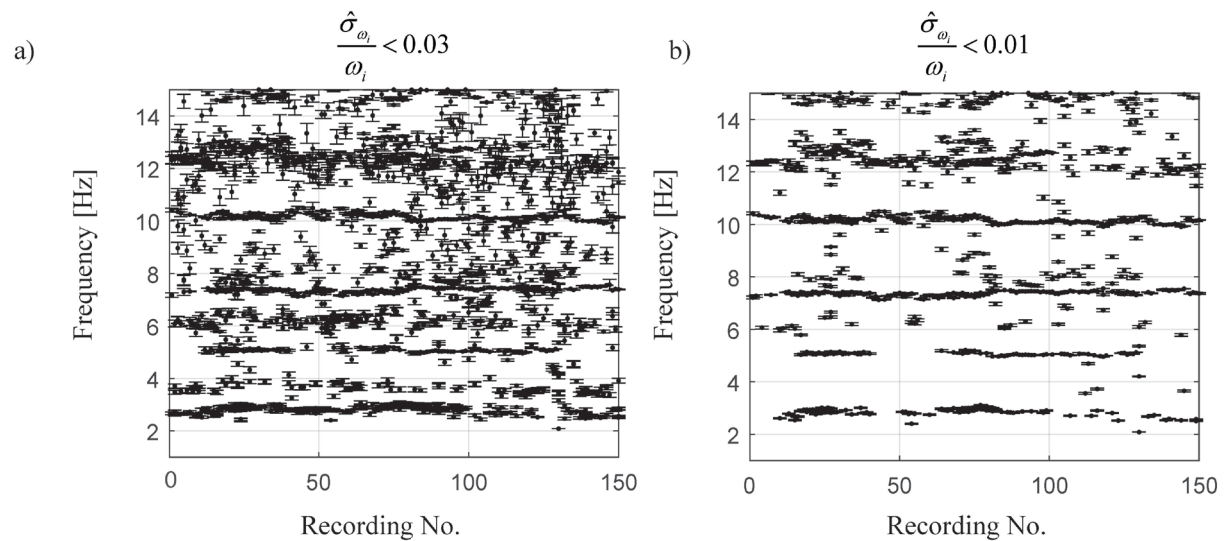


Figure 10. Accelerations measured during: crushing failure a) and b), and flexural failure c) and d).

(c) Modal parameters and their uncertainty

The measured data were used in conjunction with the automatic routine for identifying the modal parameters and their uncertainties. The automatic routine involved recordings of 17800 sample points, sampling frequency of 30 Hz and the same input values as for the simulated examples in Figure 8. The identified eigenfrequencies and corresponding standard deviations are shown in Figure 11a. A collection of points forms horizontal branches, indicating the eigenfrequencies at approximately 2.9, 5.0, 7.5 and 10.2 Hz. A scatter of points with somewhat higher standard deviations is displayed between these horizontal lines. Assuming that these are not true eigenfrequencies of the lighthouse, another attempt is made to eliminate these by lowering the tolerance value $\frac{\hat{\sigma}_{\omega_i}}{\omega_i}$ for the stabilization criterion, now set as 0.01. The horizontal branches are more pronounced as much of the scatter is successfully eliminated via the tolerance value (Figure 11b), and another branch becomes apparent at approximately 12.4 Hz.



414
415 Figure 11. Identified frequencies and their uncertainties for each recording with two different tolerance values
416 for the stabilization criterion: a) tolerance criterion $\frac{\hat{\sigma}_{\omega_i}}{\omega_i} < 0.03$, and b) tolerance criterion $\frac{\hat{\sigma}_{\omega_i}}{\omega_i} < 0.01$.

417 Figure 12 displays the identified damping obtained from the poles used to extract the eigenfrequencies in
418 Figure 11b. Large variations can be observed between the identified damping at frequencies corresponding to
419 eigenmodes 1 and 5 (approximately 2.9 Hz and 12.4Hz, respectively) and the damping identified for the other
420 eigenmodes (at 5.0, 7.5 and 10.2 Hz, respectively). The eigenmodes 1 and 5 have significantly higher damping
421 than the other eigenmodes. A possible explanation for this observation may be that eigenmodes 1 and 5 play a
422 more active role in the interaction between the ice and structure than the other eigenmodes do. Similar scatters
423 can commonly be observed for wind-sensitive bridges, for which it is well established that the modal damping
424 varies with the wind velocity (38). High damping was also estimated during laboratory model-scale ice-
425 structure interaction, where damping as high as 13 % was identified during ice crushing (18). Another
426 hypothesis considers the data quality, which may be inadequate for damping estimates for low excitation
427 amplitudes. However, these hypotheses require verification with higher quality data.

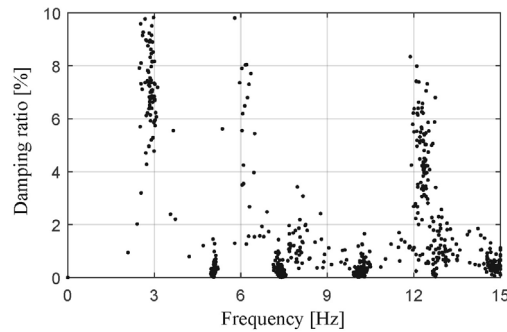


Figure 12. Identified damping for all recordings (tolerance criterion $\frac{\hat{\sigma}_{\omega_i}}{\omega_i} < 0.01$)

Since the recordings were categorised according to the governing interaction mode, it was possible to investigate differences between the identified quantities for different interaction modes. The two interaction modes, crushing and flexural failure, excited the most frequencies (Figure 13). When the ice rested against the structure (creep, Figure 13), higher eigenmodes at 5.0, 7.5 and 10.2 Hz were excited for most recordings, whereas no eigenfrequencies were identified at around the first eigenmode at 2.9 Hz, and only a few were identified in the vicinity of 12.4 Hz. These observations support the hypothesis that the eigenmodes at 2.9 Hz and 12.4 Hz participate in the interaction process at the ice-structure interface, thereby causing higher damping. It is also suggested that eigenmodes 2, 3 and 4 are less affected by both the interaction process at the ice-structure interface and the support provided from the ice resting against the structure.

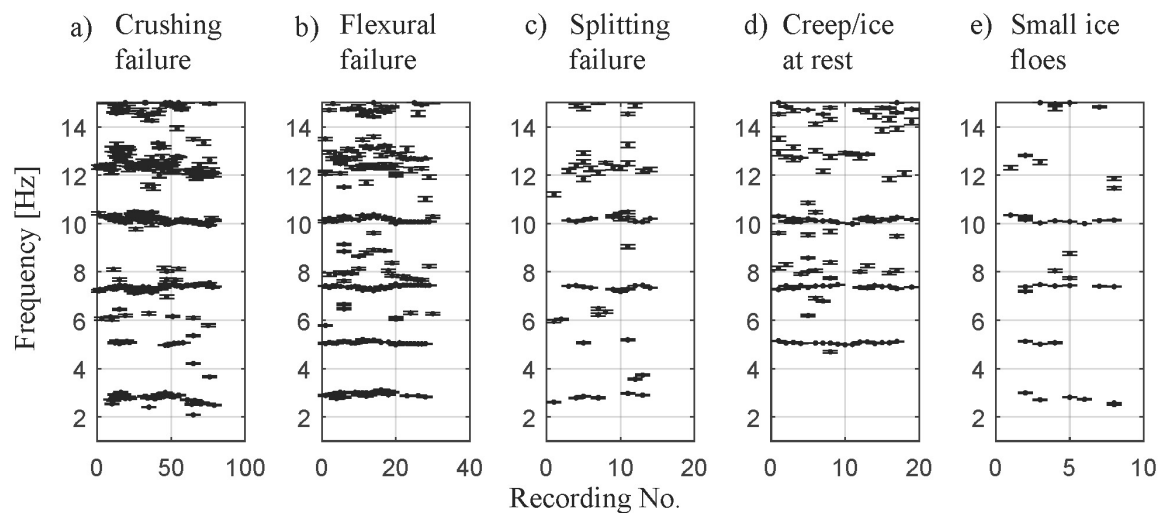


Figure 13. Frequencies identified from the automatically selected poles for different regimes of ice-structure interaction: a) crushing failure; b) flexural failure c) splitting failure; d) creep and e) floe ice.

1
2
3
4
5
6
7
8 444 The horizontal branches formed by frequencies in Figures 11 and 13 indicate the eigenfrequencies. These
9 445 branches barely resemble straight lines. Laboratory experiments of ice-induced vibrations show that the
10 446 frequency content of the structural response could be dominated by different modes of the structure
11 447 depending on the ice velocity (39). In full-scale, the ice velocity near a structure may change in a matter of
12 448 seconds, thereby influencing the governing failure mode and thus the structural response (40). The observed
13 449 variability in the results may also be explained by the differences in the ice thickness, ice-drift direction,
14 450 mechanical properties of the ice, air temperature, ice rubble accumulation at the structure, or other met-ocean
15 451 conditions that in turn cause differences in the structural behaviour.

16 452 The numerical simulations were limited to a specific mode of interaction, namely continuous brittle crushing.
17 453 In the full-scale measurements, it is important to note that even if a failure mode governed the process for
18 454 each recording, other failure mechanisms were often involved in the process. For instance, some local crushing
19 455 often took place during interactions governed by flexural failure, and even for short time sequences, the
20 456 interactions were entirely governed by crushing failure. This led to a non-stationary force and response,
21 457 possibly contributing to the observed scatter in the experimental results. Presently models for predicting
22 458 dynamic response in such mixed-mode scenarios are limited to the combination of ice crushing and buckling
23 459 (41).

24 460 Even though the structure is almost symmetric, there may be differences in the modes depending on the
25 461 direction of excitation. The recordings ranging from 23-30 in Figure 13b display identified frequencies that
26 462 resemble straight lines. For all these recordings, the interaction was governed by flexural failures, the ice-drift
27 463 direction was from south to south-southwest and the air temperature was warmer than -2°C .

28 464 Attempts were made to test whether the data were inaccurate at low vibration amplitudes by sorting out
29 465 the recorded events with the highest standard deviations of the acceleration; however no clear indication was
30 466 found. Similar results were also obtained using the UPC algorithm instead of the SSI-cov/ref. It is, however, a
31 467 fact that this is an imperfect axisymmetric problem with asymmetric mass distribution at the waterline caused
32 468 by the heavy force panels and varying mass distribution due to ice rubble. Further, an unknown extent of
33 469 nonlinearity is involved and the system identification is handled with only a few sensors. An attempt was also
34 470 made to investigate whether the first eigenmode had preferred mode shape alignments in the horizontal
35 471 plane. Only vague indications of the preferred directions were found, but the results highly depend on the
36 472 slack values for the automated selection of modes, and such analysis lies beyond the scope of this study. Due
37 473 to the few sensor locations, the identified mode shapes and their variances were also not considered in this
38 474 study. By using a hierarchy clustering method as described in (42), similar results as shown in Figure 11b were
39 475 obtained when low importance was assigned to the weights for the MAC-values and clusters with few poles
40 476 were discarded. It must also be noted that the identified eigenfrequencies indicate that the FE model contained

1
2
3
4
5 477 modelling errors. Updating the model would benefit numerical simulations in the future, but it does not
6 478 influence the conclusions of this study.

7 479 Nord et al. (40) studied 61 events of frequency lock-in vibrations of the Norströmsgrund lighthouse. This is
8 480 a mode of vibrations caused by crushing failure under certain conditions; lock-in vibrations have been a topic
9 481 of research during the past 50 years (43) and still represent a popular research topic. The vibrations' signature
10 482 is an amplified periodic response near one of the eigenfrequencies of the structure. For the 61 frequency lock-
11 483 in events analysed, the governing frequency of vibrations was 2.3 Hz, more than 20% lower than the
12 484 suggested eigenfrequency found in this study at 2.9 Hz, which is somewhat more than that reported for
13 485 channel markers in the Baltic Sea (44).
14
15
16
17
18
19 486

20 21 487 6. Conclusions

22
23 488 Simulated and measured recordings of a structure subjected to ice actions were used to assess the possibility
24 489 to identify consistent modal parameters during ice-structure interaction and consistent system changes with
25 490 observed ice conditions.

26 491 The combined use of ice-structure interaction simulations and identification of variances alongside modal
27 492 parameters rendered insight into how the identified modal parameters were influenced by the presence of ice.
28 493 The simulations guided the choice of tolerance values for the stabilization criterion, in turn rendering some
29 494 consistent estimates of eigenfrequencies for different ice conditions with measured data.

30 495 Even though the eigenfrequency often varied between each data recording, some consistency was noted
31 496 between the ice failure mode and identified frequencies. The lowest eigenfrequency at approximately 2.9 Hz
32 497 was identified in all interaction modes except in the case of creep, i.e., when the ice was resting against the
33 498 structure. This eigenmode, as well as another mode at 12.4 Hz, exhibited significantly higher damping than
34 499 the other eigenmodes, and these eigenmodes were mostly identified during crushing and flexural ice failures.

35 500 It is therefore suggested that these modes were influenced by the interaction process at the ice-structure
36 501 interface. Since eigenmodes at 5.0, 7.5 and 10.2 Hz were identified also during creep and had for all cases
37 502 significantly lower damping, it is suggested that these higher modes were less influenced by the interaction
38 503 process. For the sake of SHM, identifying eigenmodes insensitive to the interaction process significantly
39 504 reduces the environmental variability and may turn out useful in selecting damage-sensitive features.

40 505 The variability in the results may be explained by the violation of the underlying assumptions used to derive
41 506 the applied identification routine, the structural complexity and limited sensor data of uncertain quality.
42
43
44
45
46
47
48
49
50
51
52 507

53 508 Additional Information

54 509
55
56
57
58
59
60

Phil. Trans. R. Soc. A.

510 Data Accessibility
 511 The data accessibility is handled by the Hamburg ship model basin (HSVA).
 512 www.hsva.de

514 Authors' Contributions

516 T.S.N. performed the simulations, identifications, and data analysis, and drafted the manuscript.
 517 H.H. conducted the simulations with the ice model.
 518 Ø.W.P. performed the data analysis.

520 Funding Statement

521 The study was conducted with support from the Research Council of Norway through the Centre for
 522 Research-based Innovation SAMCoT (50049000 SAMCoT Financial Contribution Partners) and support from
 523 all SAMCoT partners (10382200 SAMCoT SFI Funding Research Council of Norway). The work is also funded
 524 by the Research Council of Norway and co-funded by European Union's Horizon 2020 research and
 525 innovation programme under the framework of ERA-NET Cofund MarTERA (Maritime and Marine
 526 Technologies for a new Era).
 527 The full-scale measurements were funded by the European Commission DG RESEARCH under the Fifth
 528 Framework Programme for Research and Development within the Energy, Environment and Sustainable
 529 Development (EESD) Programme under the Key Action RTD activities of a generic nature (Contract No.
 530 EVG1-CT-2000-00024).

532 Acknowledgments

533 The authors wish to acknowledge the support in data processing provided by Dr. Ying Tu at the Norwegian
 534 University of Science and Technology.

536 References

1. Blenkarn KA, editor Measurement and analysis of ice forces on Cook Inlet structure. Offshore Technology Conference; 1970; Houston, TX.
2. Peyton HR. Sea Ice Strength: University of Alaska; 1967.
3. Frederking R, Haynes FD, Hodgson TP, Sayed M. Static and dynamic ice loads on the Yamachiche lightpier, 1984-1986. 8th International Symposium on Ice, IAHR Iowa, USA 1986. p. 115-26.
4. Määttänen M. Experiences of ice forces against a steel lighthouse mounted on the seabed, and proposed constructional refinements. Port and Ocean Engineering under Arctic conditions (POAC); Fairbanks, Alaska 1975. p. 857-67.
5. Bjerkås M, Nord TS. Ice action on Swedish lighthouses Revisited. The 23rd IAHR International symposium on ice; Ann Arbor, Michigan, USA 2016.
6. Timco G, Croasdale KR. How well can we predict ice loads? IAHR; Sapporo, Japan 2006. p. 167-74.
7. Danys JV. Ice forces on old and new offshore lighthouses in the St. Lawrence Waterway. Port and Ocean Engineering under Arctic Conditions (POAC); St. Johns, Newfoundland, Canada 1977. p. 115-38.
8. Määttänen M, Kärnä T. ISO 19906 ice crushing load design extension for narrow structures. Proceedings of the 21st International Conference on Port and Ocean Engineering under Arctic Conditions (POAC); Montréal, Canada 2011.
9. Bjørk B. Ice-induced Vibration of Fixed Offshore Structures. Part 2: Experience with Baltic Lighthouses: Ship Research Institute of Norway, Information Department; 1981.

58 *Phil. Trans. R. Soc. A.*

10. Hendrikse H, Metrikine A. Interpretation and prediction of ice induced vibrations based on contact area variation. *International Journal of Solids and Structures*. 2015;75–76:336-48.
11. Määttänen M. On conditions for the rise of self-excited ice induced autonomous oscillations in slender marine pile structures [PhD]: UNIVERSITY OF OULU; 1978.
12. Sodhi DS. Ice-induced vibration of structures. *Proceedings of the 9th IAHR International Symposium on Ice; Sapporo, Japan 1988*. p. 625-57.
13. Jefferies MG, Wright WH. Dynamic response of "Molikpaq" to ice-structure interaction. *Proc 7th International conference on Offshore Mechanics and Arctic Engineering (OMAE 88); Houston, Texas, United States 1988*. p. 201-20.
14. Londoño NA. Use of vibration data for structural health monitoring of Bridges. Ottawa: Carleton University; 2006.
15. Brown TG, Tibbo JS, Tripathi D, Obert K, Shrestha N. Extreme ice load events on the Confederation Bridge. *Cold Regions Science and Technology*. 2010;60(1):1-14.
16. Shrestha N, Brown TG. 20 years of monitoring of ice action on the Confederation Bridge piers. *Cold Regions Science and Technology*. 2018;151:208-36.
17. Hendrikse H, Metrikine A, Evers K-U. A method to measure the added mass and added damping in dynamic ice-structure interaction. "Ice Research for a Sustainable Environment"(IAHR) Dalian, China Paper no 094 2012.
18. Singh SK, Timco GW, Frederking R, Jordaan IJ. Tests of ice crushing on a flexible structure. *OMAE Houston TX. USA 1990*. p. 89-94.
19. Hendrikse H. Ice-induced vibrations of vertically sided offshore structures: Delft University of Technology; 2017.
20. Nord TS, Kvåle KA, Petersen ØW, Bjerkås M, Lourens E-M. Operational modal analysis on a lighthouse structure subjected to ice actions. *Procedia Engineering*. 2017;199:1014-9.
21. Reynders E, Pintelon R, De Roeck G. Uncertainty bounds on modal parameters obtained from stochastic subspace identification. *Mechanical Systems and Signal Processing*. 2008;22(4):948-69.
22. Döhler M, Mevel L. Efficient multi-order uncertainty computation for stochastic subspace identification. *Mechanical Systems and Signal Processing*. 2013;38(2):346-66.
23. Jordaan IJ. Mechanics of ice–structure interaction. *Engineering Fracture Mechanics*. 2001;68(17–18):pp.1923-60.
24. Kärnä T, Jochmann P. Field observations on failure modes. *Port and Ocean Engineering under Arctic Conditions; Trondheim, Norway 2003*. p. 839-49.
25. Wells J, Jordaan I, Derradji-Aouat A, Taylor R. Small-scale laboratory experiments on the indentation failure of polycrystalline ice in compression: Main results and pressure distribution. *Cold Regions Science and Technology*. 2011;65(3):pp. 314-25.
26. Nord TS, Øiseth O, Lourens E-M. Ice force identification on the Norströmsgrund lighthouse. *Computers & Structures*. 2016;169(Supplement C):24-39.
27. Peeters B, De Roeck G. Reference-based stochastic subspace identification for output-only modal analysis. *Mechanical Systems and Signal Processing*. 1999;13(6):855-78.
28. Reynders E, Maes K, Lombaert G, De Roeck G. Uncertainty quantification in operational modal analysis with stochastic subspace identification: Validation and applications. *Mechanical Systems and Signal Processing*. 2016;66-67:13-30.
29. Mellinger P, Döhler M, Mevel L. Variance estimation of modal parameters from output-only and input/output subspace-based system identification. *Journal of Sound and Vibration*. 2016;379:1-27.
30. Döhler M, Lam X-B, Mevel L. Uncertainty quantification for modal parameters from stochastic subspace identification on multi-setup measurements. *Mechanical Systems and Signal Processing*. 2013;36(2):562-81.
31. ISO. ISO/FDIS 19906. 2010. p. 188.
32. Sodhi D, Haehnel R. Crushing Ice Forces on Structures. *Journal of Cold Regions Engineering*. 2003;17(4):153-70.
33. Hendrikse H, Nord TS. Dynamic response of an offshore structure interacting with an ice floe failing in crushing. *Marine Structures*. 2019;65:271-90.

34. Hendrikse H. Model for simulation of dynamic ice-structure interaction for vertically sided offshore structures - SDOF MATLAB implementation. Mendeley Data v2, <https://data.mendeley.com/datasets/582m8565dj/2>, 2019.
35. Heinonen J, Kärnä T, Luo C. Dynamic Behavior of the Nordströmsgrund Lighthouse, STRICE-REPORT. VTT Technical Research Centre of Finland and Luleå University of Technology; 2003.
36. Jochmann P, Schwarz J. Ice force measurements at lighthouse Norströmsgrund- winter 1999, LOLEIF Report No. 5, MAS3-CT-97-0098. Hamburgische schiffbau-versuchsanstalt GmbH; 1999.
37. Bjerkås M. Ice action on offshore structures [PhD]: NTNU, ISBN 82-471-7756-0; 2006.
38. Hong AL, Ubertini F, Betti R. Wind Analysis of a Suspension Bridge: Identification and Finite-Element Model Simulation. Journal of Structural Engineering. 2011;137(1):133-42.
39. Nord TS, Øiseth O, Lourens E, Määttänen M, Høyland KV. Laboratory experiments to study ice-induced vibrations of scaled model structures during their interactions with level ice at different ice velocities. Cold Regions Science and Technology. 2015(119):1-15.
40. Nord TS, Samard ija I, Hendrikse H, Bjerkås M, Høyland KV, Li H. Ice-induced vibrations of the Norströmsgrund lighthouse. Cold Regions Science and Technology. 2018;155:237-51.
41. Hendrikse H, Metrikine A. Ice-induced vibrations and ice buckling. Cold Regions Science and Technology. 2016;131:129-41.
42. Magalhães F, Cunha Á, Caetano E. Online automatic identification of the modal parameters of a long span arch bridge. Mechanical Systems and Signal Processing. 2009;23(2):316-29.
43. Määttänen M. Ice induced frequency lock-in vibrations - Coverging towards consensus. Proceedings of the 23rd International Conference on Port and Ocean Engineering under Arctic Conditions; Trondheim, Norway 2015.
44. Kärnä T. Steady-state vibrations of offshore structures. Hydrotechnical Construction. 1994;28(8):446-53.

Tables

Table 1. Modal properties of simulation model.

	Mode 1 (2)	Mode 3 (4)	Mode 5 (6)	Mode 7 (8)
f_i [Hz]	2.465	3.920	5.516	10.162
ξ_i [%]	2.000	2.005	2.367	3.642

Table 4. Identified modal parameters, their uncertainties and percentage errors.

Identified eigenmodes	White noise $f_i \pm \hat{\sigma}_{f_i}$ (Hz) / (error (Hz))	Slow-varying ice conditions $f_i \pm \hat{\sigma}_{f_i}$ (Hz) / (error (Hz))	Fast-varying ice conditions $f_i \pm \hat{\sigma}_{f_i}$ (Hz) / (error (Hz))
Mode 1	2.465 ± 0.004 / (0.000)	2.454 ± 0.005 / (0.011)	2.462 ± 0.005 / (0.003)
Mode 2	3.923 ± 0.010 / (0.003)	3.925 ± 0.027 / (0.005)	3.909 ± 0.021 / (0.011)
Mode 3	5.517 ± 0.051 / (0.001)	5.527 ± 0.057 / (0.011)	5.505 ± 0.068 / (0.011)

Mode 4	$10.148 \pm 0.134 / (0.014)$	$10.173 \pm 0.121 / (0.011)$	$10.140 \pm 0.072 / (0.022)$
	White noise	Slow-varying ice conditions	Fast-varying ice conditions
	$\xi_i \pm \hat{\sigma}_{\xi_i} (\%) / (error \%)$	$\xi_i \pm \hat{\sigma}_{\xi_i} (\%) / (error \%)$	$\xi_i \pm \hat{\sigma}_{\xi_i} (\%) / (error \%)$
Mode 1	$2.149 \pm 0.193 / (0.149)$	$1.627 \pm 0.215 / (0.373)$	$1.804 \pm 0.211 / (0.196)$
Mode 2	$1.793 \pm 0.266 / (0.212)$	$2.239 \pm 0.653 / (0.391)$	$2.070 \pm 0.619 / (0.065)$
Mode 3	$2.623 \pm 0.726 / (0.256)$	$2.092 \pm 0.837 / (0.275)$	$2.188 \pm 0.867 / (0.178)$
Mode 4	$3.840 \pm 0.961 / (0.198)$	$3.438 \pm 0.975 / (0.204)$	$3.566 \pm 0.635 / (0.075)$

Table 5. Natural frequencies and damping ratios of the first identified mode. μ_{f_i} and μ_{ξ_i} : mean values over 250 simulations. $\hat{\sigma}_{f_i}^2$ and $\hat{\sigma}_{\xi_i}^2$: mean of the estimated variances. $\sigma_{f_i}^2$ and $\sigma_{\xi_i}^2$: empirical sample variances.

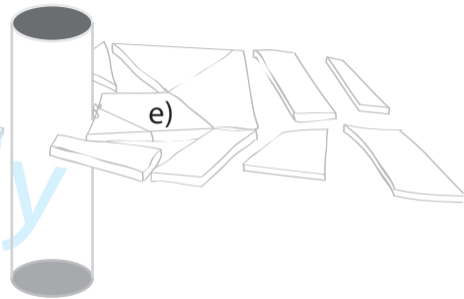
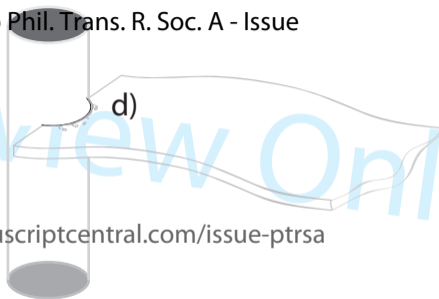
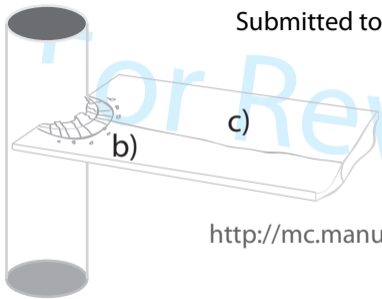
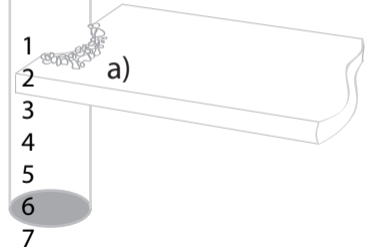
Mode	μ_{f_i} (Hz)	$\hat{\sigma}_{f_i}^2$	$\sigma_{f_i}^2$	μ_{ξ_i} (%)	$\hat{\sigma}_{\xi_i}^2$	$\sigma_{\xi_i}^2$
Mode 1 (ice-structure interaction)	2.459	$1.153 \cdot 10^{-2}$	$1.202 \cdot 10^{-1}$	1.530	$8.096 \cdot 10^{-1}$	$4.288 \cdot 10^{-1}$
Mode 1 (white noise input)	2.465	$4.999 \cdot 10^{-3}$	$4.857 \cdot 10^{-3}$	2.047	$2.152 \cdot 10^{-1}$	$1.977 \cdot 10^{-1}$
Mode 1 (ice-structure interaction) Short time series	2.433	$2.317 \cdot 10^{-2}$	$5.887 \cdot 10^{-2}$	1.859	1.864	$4.035 \cdot 10^{-1}$
Mode 1 (white noise input) Short time series	2.464	$1.598 \cdot 10^{-2}$	$4.577 \cdot 10^{-3}$	2.004	$7.992 \cdot 10^{-1}$	$1.977 \cdot 10^{-1}$

Figure and table captions

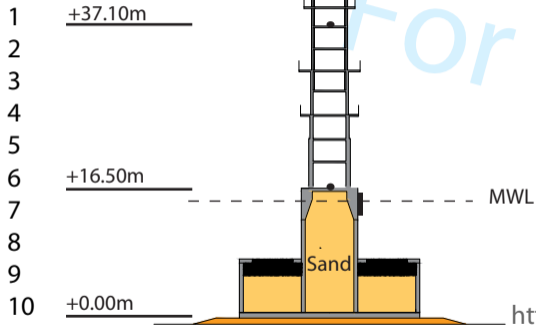
Figure 1. Types of failure modes of ice-structure interaction (from Nord et al. (20)). 4

Phil. Trans. R. Soc. A.

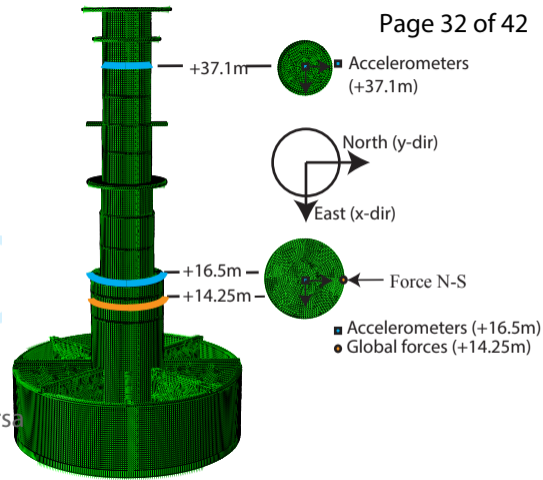
1		
2		
3		
4		
5		
6	Figure 2. Illustration, picture and finite element model of the Norströmsgrund lighthouse, from Nord et al.	
7		
8	(26).....	10
9	Figure 3. Mode shapes and corresponding natural frequencies of the finite element model (From Nord et al.	
10	(26)).....	10
11	Figure 4. Simulated force time histories during interaction with slow-varying (top figure) and fast-varying	
12	(bottom) ice conditions.	12
13	Figure 5. Stabilization diagrams for a) slow-varying ice conditions b) fast-varying ice conditions.	14
14	Figure 6. Ice force spectrum used for monte-carlo simulations.	15
15	Figure 7. Identified frequencies and their uncertainties for each simulation with a) ice-structure interaction,	
16	and b) Gaussian white noise input. Each simulation contained $N=59000$ sample points.....	17
17	Figure 8. Identified frequencies and their uncertainties for each simulation with a) ice-structure interaction,	
18	and b) Gaussian white noise input. Each simulation contained $N=17800$ sample points.....	18
19	Figure 9. The Norströmsgrund lighthouse during ice action: a) rubble formation after ice interaction (Photo by	
20	courtesy of Basile Bonnemaire); b) crushing ice failure and c) splitting ice failure.....	19
21	Figure 10. Accelerations measured during: crushing failure a) and b), and flexural failure c) and d).....	20
22	Figure 11. Identified frequencies and their uncertainties for each recording with two different tolerance values	
23	for the stabilization criterion: a) tolerance criterion $\frac{\hat{\sigma}_{\omega_i}}{\omega_i} < 0.03$, and b) tolerance criterion $\frac{\hat{\sigma}_{\omega_i}}{\omega_i} < 0.01$	21
24		
25	Figure 12. Identified damping for all recordings (tolerance criterion $\frac{\hat{\sigma}_{\omega_i}}{\omega_i} < 0.01$)	22
26		
27	Figure 13. Frequencies identified from the automatically selected poles for different regimes of ice-structure	
28	interaction: a) crushing failure; b) flexural failure c) splitting failure; d) creep and e) floe ice.	22
29		
30		
31	Table 1. Modal properties of simulation model.	
32	Table 2. Identified modal parameters (using SSI-cov/ref), standard deviations and absolute errors.	
33	Table 3. Natural frequencies and damping ratios of the first identified eigenmode. μ_{f_i} and μ_{ξ_i} : mean values	
34	over 250 simulations. $\hat{\sigma}_{f_i}$ and $\hat{\sigma}_{\xi_i}$: mean of the estimated standard deviations. σ_{f_i} and σ_{ξ_i} : sample standard	
35	deviation.	
36		
37		
38		
39		
40		
41		
42		
43		
44		
45		
46		
47		
48		
49		
50		
51		
52		
53		
54		
55		
56		
57		
58		
59	<i>Phil. Trans. R. Soc. A.</i>	
60		



• Accelerometers
| Force panel



<http://mc.manuscriptcentral.com/issue-ptrsa>



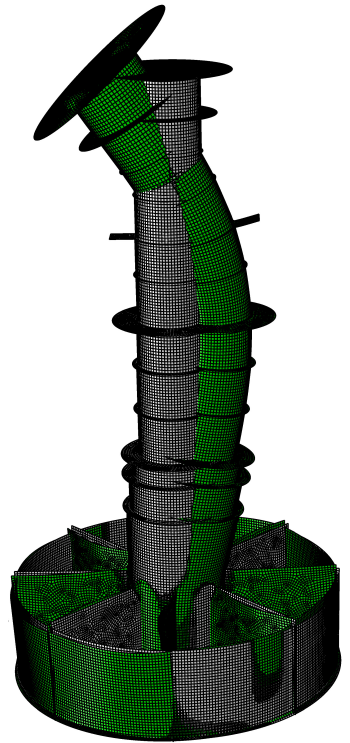
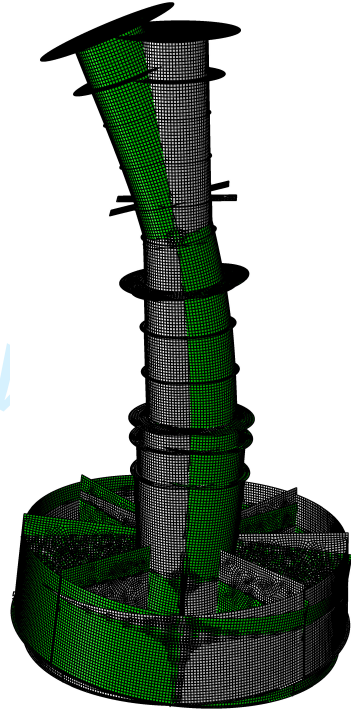
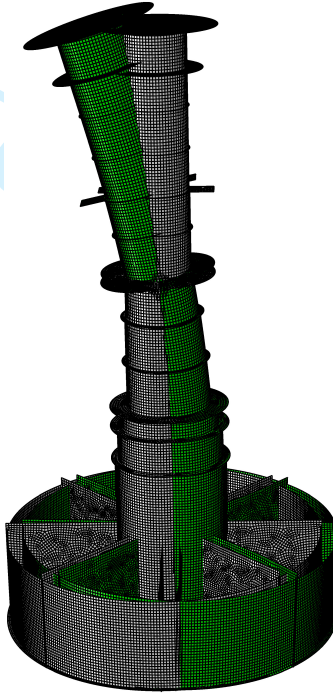
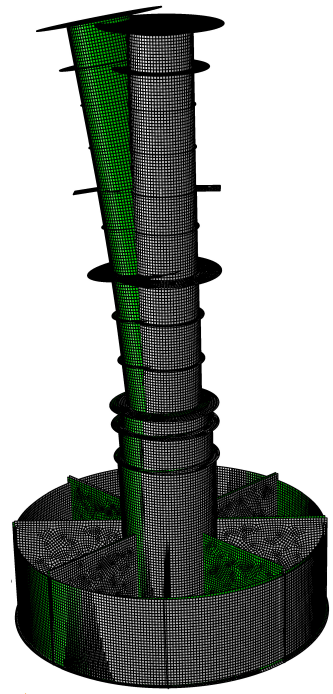
Mode 1 (2)
2.465 Hz

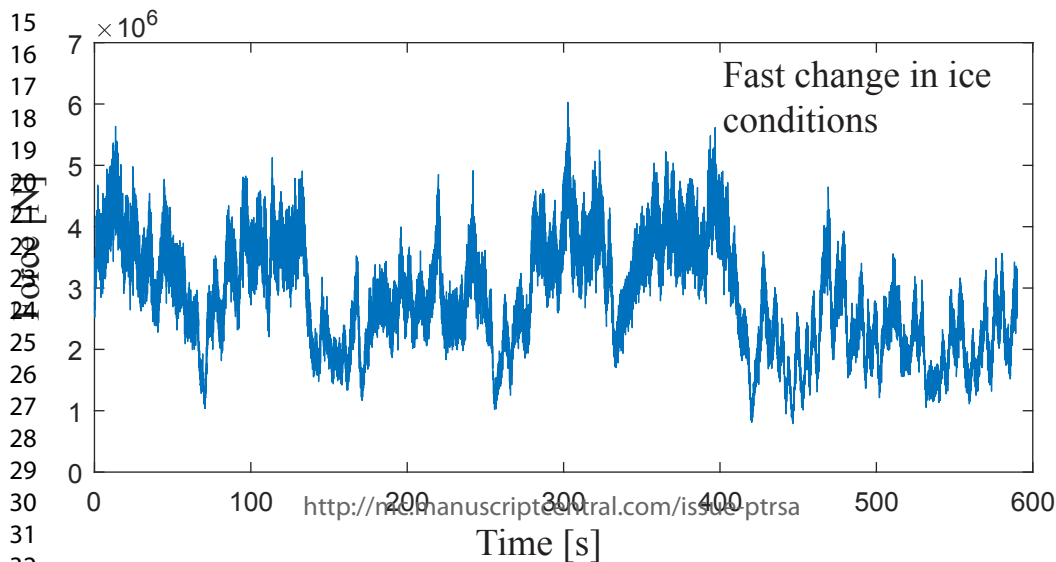
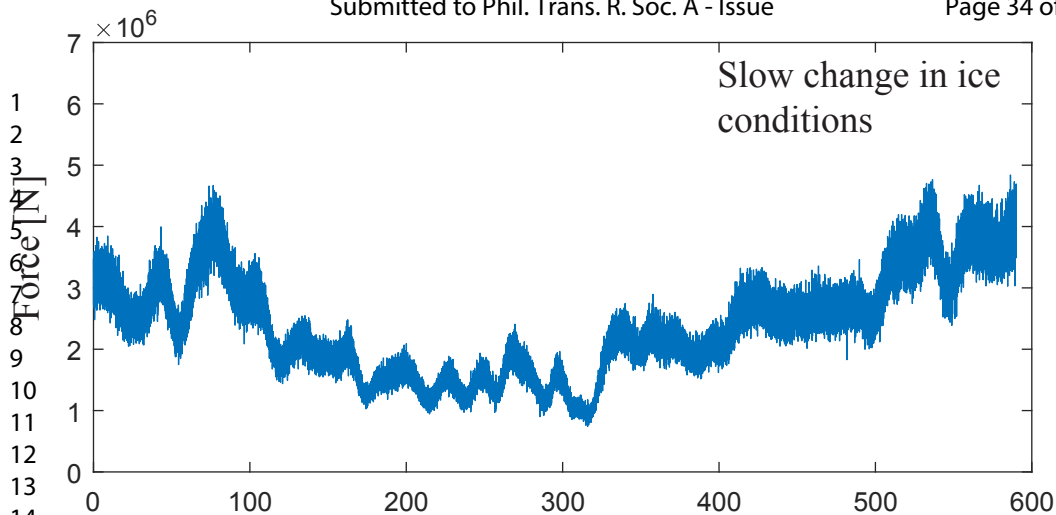
Mode 3 (4)
3.920 Hz

Mode 5 (6)
5.516 Hz

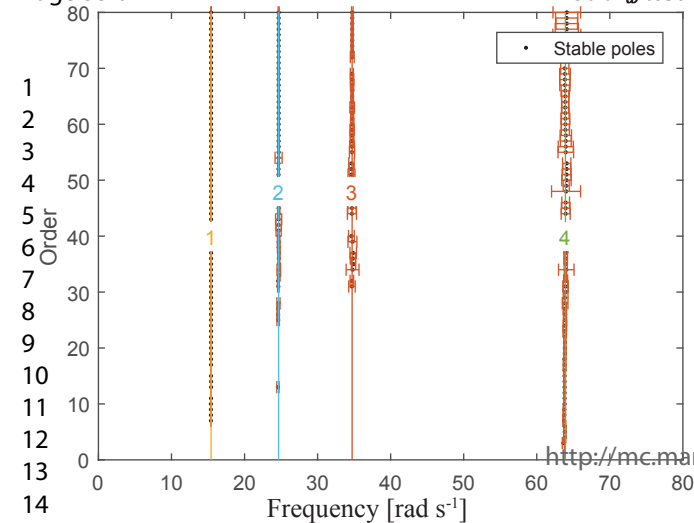
Mode 7 (8)
10.162 Hz

1
2
3
4
5
6
7
8
9
10
11
12
13
14
15
16
17
18
19
20
21
22
23
24
25
26
27

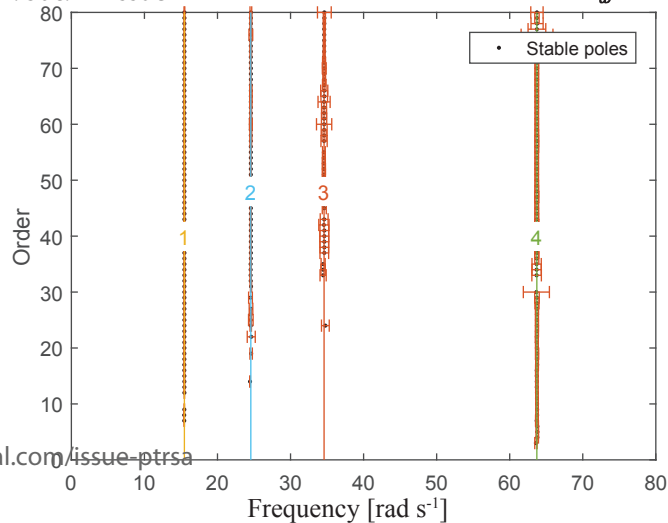




1 x stability
a) Criteria: $\Delta\omega/\omega < 1\%$ and $\Delta\xi/\xi < 5\%$ MAC > 95% and $\sigma_\omega/\omega < 0.05$

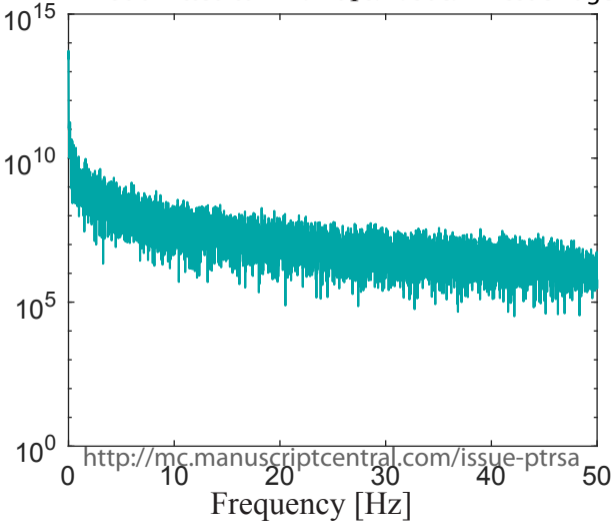


1 x stability
b) Criteria: $\Delta\omega/\omega < 1\%$ and $\Delta\xi/\xi < 5\%$ MAC > 95% and $\sigma_\omega/\omega < 0.05$



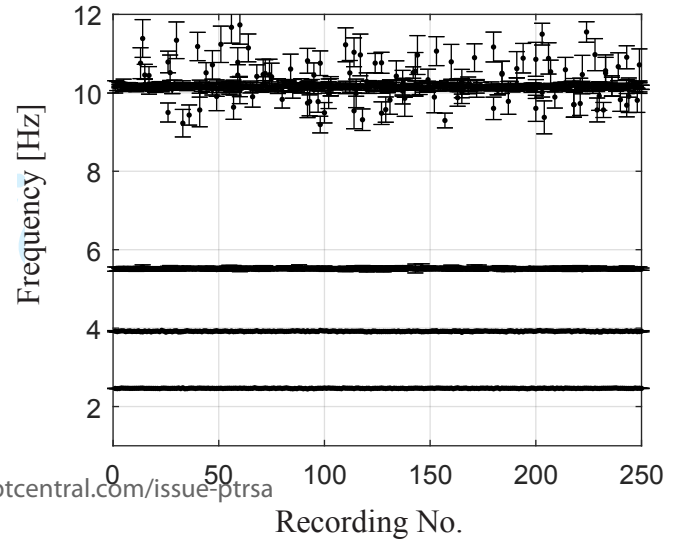
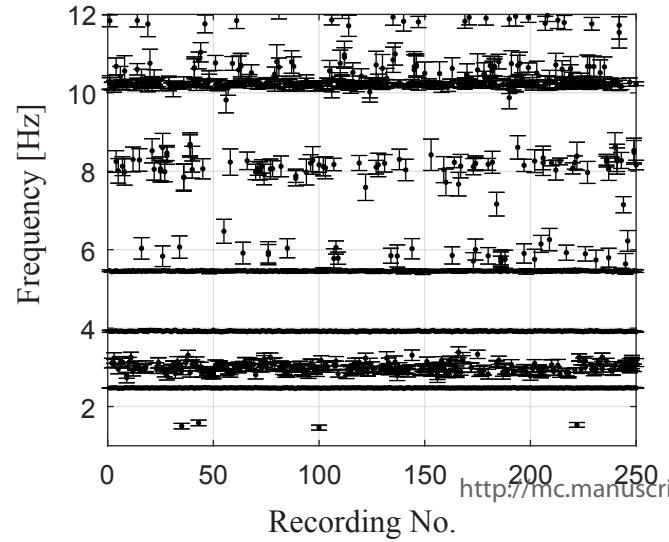
Ice force spectrum

1
2
3
4
5
6
7
8
9
10
11
12
13
14
15



a) Ice-structure interaction

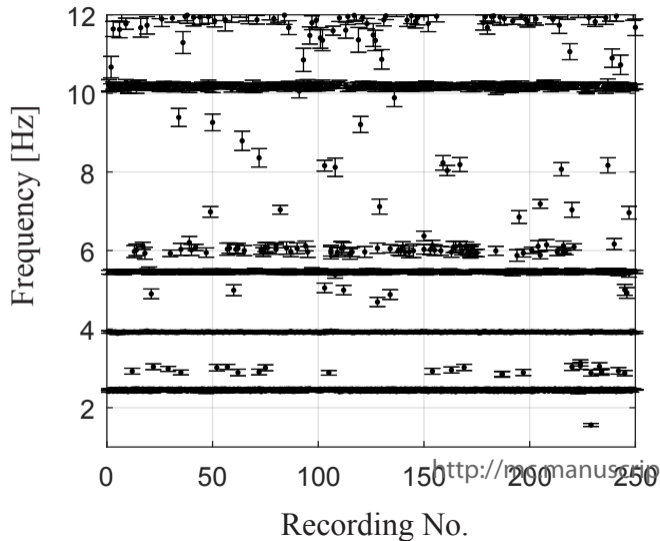
b) Gaussian white noise input



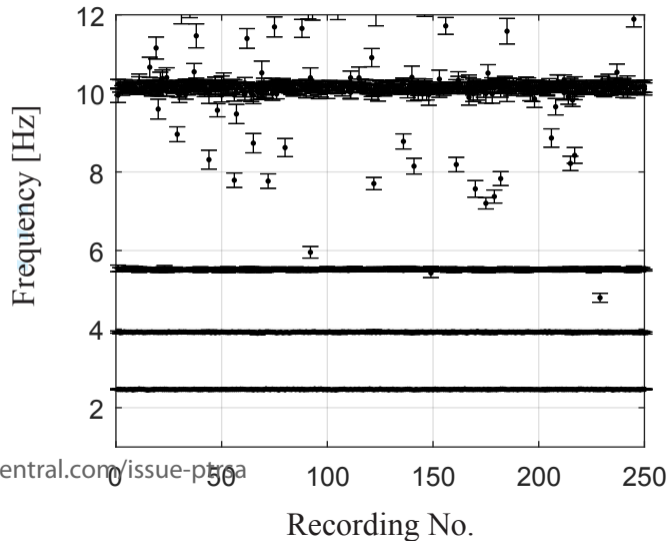
1
2
3
4
5
6
7
8
9
10
11
12
13
14
15
16
17

a)

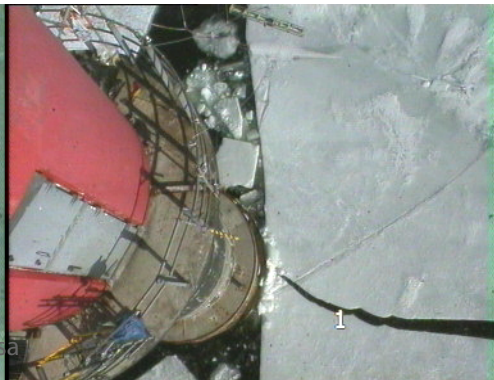
Ice-structure interaction



Gaussian white noise input

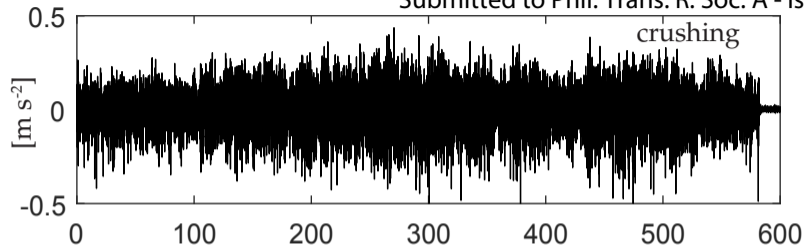


1
2
3
4
5
6
7
8
9
10
11
12
13

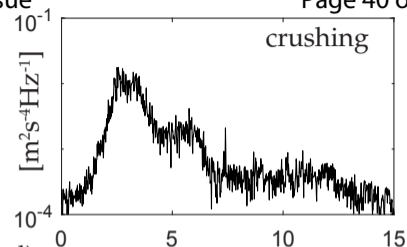


<https://www.manuscriptcentral.com/issue-ptrsa>

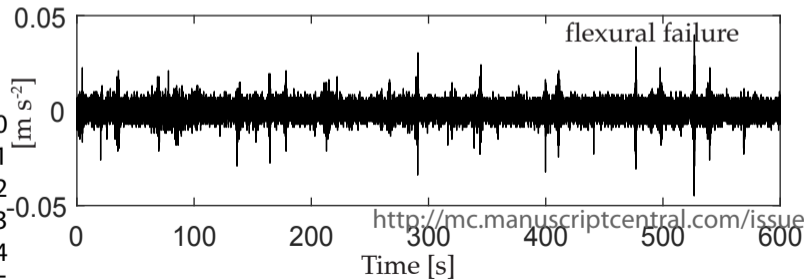
a)



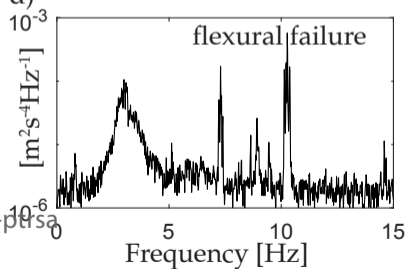
b)

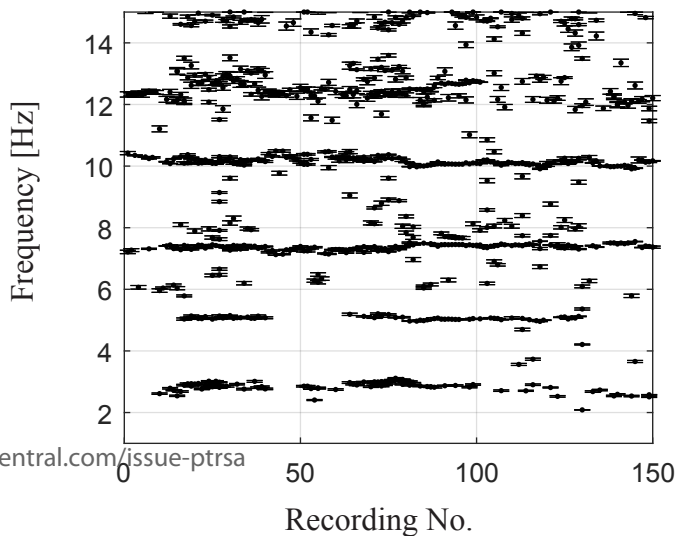
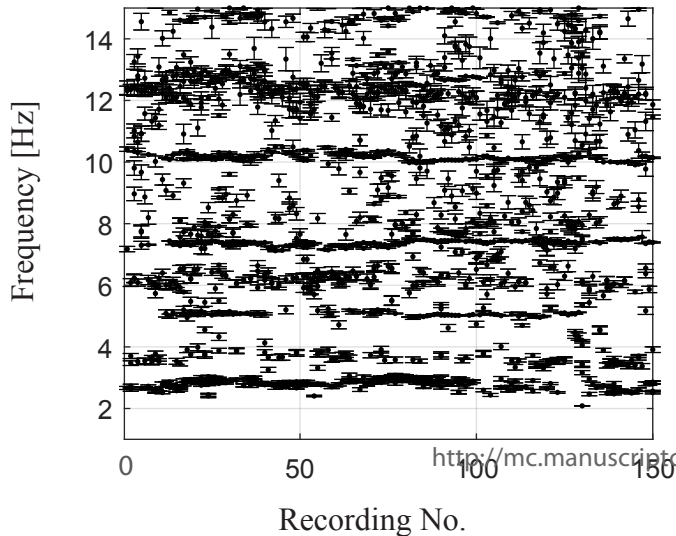


c)



d)



1
2
3
4
5
6
7
8
9
10
11
12
13
14
15
16
17

a) Crushing failure

b) Flexural failure

c) Splitting failure

d) Creep/ice at rest

e) Small ice floes

